J. Iron Steel Res. Int. (2023) 30:193–215
https://doi.org/10.1007/s42243-022-00872-7

REVIEW

Progress in corrosion-resistant coatings on surface of low alloy steel

Bao-sheng Liu[1] · Jia-li Li[1] · Wen-jie Guo[1] · Peng-fei Xu[1] · Shao-hua Zhang[1] · Yue-zhong Zhang[2]

Received: 3 January 2022 / Revised: 4 May 2022 / Accepted: 10 May 2022 / Published online: 19 December 2022

Abstract
Low alloy steels are widely used in bridges, construction, chemical and various equipment and metal components due to their low cost and excellent mechanical strength. Information in the literature related to the preparation, advantages and disadvantages, and applications along with research progress of various types of protective coatings suitable for low-alloy steel surfaces is reviewed, while a conclusive and comparative analysis is also afforded to the numerous factors influencing the protective ability of coatings. The characteristics of coatings drawn from the latest published literature are discussed and suggest that the modification of traditional metal coatings and the development of new organic coatings under the consideration of environmental protection, low cost, simplicity and large-scale industrial application are simultaneously proceeding, which holds promise for improving the understanding of corrosion protection in related fields and helps to address some of the limitations identified with more conventional coating techniques.

Keywords Low alloy steel · Corrosion-resistant coating · Metal coating · Composite coating · Diffusion coating · Organic coating

1 Introduction

Low alloy steel, the most commonly used structural engineering materials, is widely used in bridges, construction, petrochemical and various equipment along with metal components due to its low cost and excellent mechanical strength [1–3]. Unfortunately, the occurrence of accelerated corrosion and/or chemical degradation failures of low alloy steel is prevalent since its surface is inevitable to contact with the corrosive media from atmosphere, water, soil as well as other environments during the long-term service condition, which contributes greatly to the non-structural catastrophes and economic losses [4]. Thus, it is a great challenge to improve the corrosion resistance of low alloy steel and extend its life and application range in various service environments [5–7], through which the conservation/protection of energy resources and environment, along with maintenance of production and life safety, is well achieved. There have been a number of papers published within the area of the corrosion resistance of low alloy steel over the last two decades, and the anti-corrosion measurements for low-alloy steel mainly focus on alloying and surface treatment [8, 9], in which alloying refers to adding relatively small amounts of alloying elements into the steel to obtain a "stainless" material with excellent corrosion resistance. However, this technique is always restricted by increased costs and complicated production processes under the consideration of the corrosion processes mainly occurring on the metal surface. In comparison, the coating technique is an effective method improving the service life of the steel, and a broad spectrum of coatings on the steel surface not only offers greater corrosion resistance than that of the alloying techniques, but is also responsible for its economic aspects and additional functionalization [10, 11]. Considering a diffusion-barrier effect on electrochemically active species followed by blocking active sites on the steel surface, the coatings are capable of defining/reducing the corrosion rate of the underlying steel by well over an order of magnitude.

✉ Bao-sheng Liu
liubaosheng@tyust.edu.cn

✉ Shao-hua Zhang
zhangshaohua@tyust.edu.cn

[1] College of Materials Science and Engineering, Taiyuan University of Science and Technology, Taiyuan 030024, Shanxi, China

[2] College of Chemical Engineering and Technology, Taiyuan University of Science and Technology, Taiyuan 030024, Shanxi, China

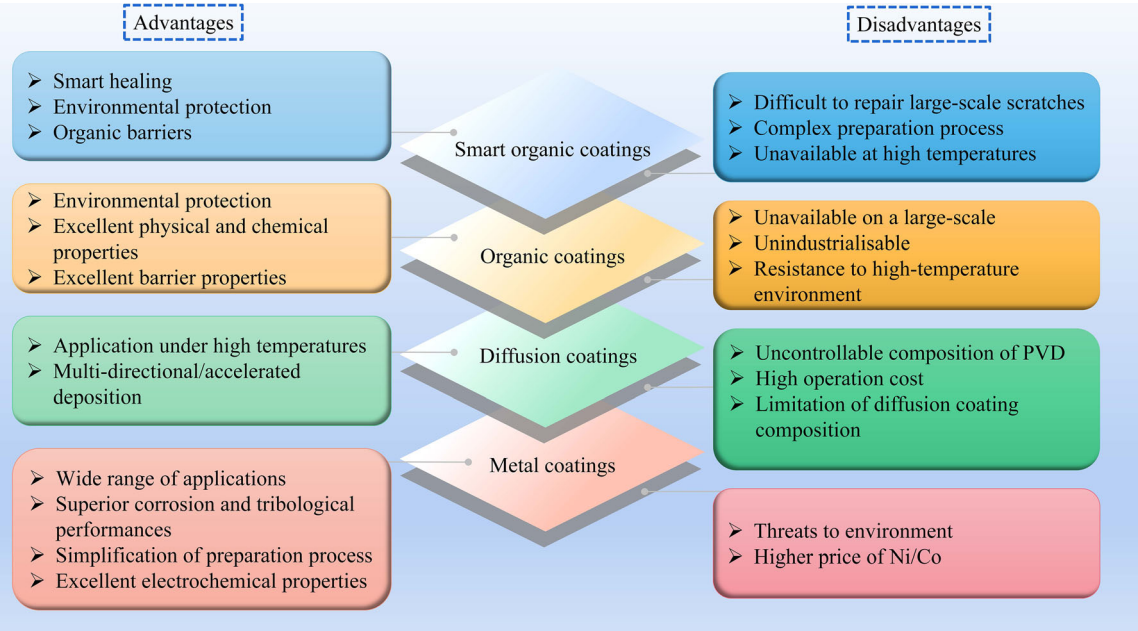

Fig. 1 Advantages and disadvantages of metal coatings, diffusion coatings, organic coatings and smart organic coatings

Consequently, it is critical to set up a fundamental understanding regarding the preparation methods, properties and advances of various types of protective coatings. Despite the existence of a significant body of review literature within the area of coatings over the last two decades, e.g., metal coatings [12, 13], diffusion coatings [14, 15], organic coatings [16, 17], smart coatings [18, 19] and a series of composite coatings [20, 21] (the simple summary of advantages and disadvantages for these protective coatings is shown in Fig. 1), and accordingly associated with a series of coating technologies involving electroplating and electroless plating [22], physical vapor deposition (PVD) [23], chemical vapor deposition (CVD) [24], laser cladding [25], plasma spray welding [26], thermal spraying [27, 28], hot dip coating [29] and so on, some of these methods do not completely qualify for low alloy steel and/or diverse use at industrial-scale or under harsh conditions.

This review paper focuses exclusively on consolidating the information related to the corrosion-resistant coatings and the corresponding techniques that are suitable for the protection of low alloy steel based on the recently published literature, and an effort has been made herein to review and/or compare in detail preparation method, application and advantages/disadvantages, while a conclusive and comparative analysis is also afforded to numerous factors influencing the protective ability of coatings and its purpose is to improve the understanding of corrosion protection in related fields and help to address some of limitations identified with more conventional coating techniques.

2 Metal and composite coatings

2.1 Metal coatings

Metal coatings are currently one of the most suitable methods for surface protection of low alloy steel and have been widely employed in industrial fields [12, 13], such as aviation, metallurgy, chemical industry, automotive transport and other fields due to their high wear/corrosion resistance and electrical properties. Before discussing the types of metal coatings, it is perhaps prudent to conclude the fundamental coating techniques that correspond to the metal coatings, which mainly include electroplating, electroless plating, thermal spraying, PVD, CVD and laser cladding [22–29]. Electroplating offers numerous advantages, such as a precise control over thickness and microstructure of the film, moderate cost, facile application, and a low operating temperature. At the initial stage of coating development, electroplating chromium coatings on the surface of low alloy steel has been widely used in industrial fields. In spite of these benefits, some technical and environmental obstacles involve cracks in the microstructure, hydrogen embrittlement performance and especially the irreversible release of toxic Cr^{3+}/Cr^{6+}, causing serious threats to human and environment health [30], which acts as a principal driving force behind the need to secure acceptable alternatives to Cr metal coatings.

Since the twentieth century, many attempts have been devoted to alternatives to chromium, as a general classification of Ni/Co-based alloy and composite electrodeposits,

e.g., Ni–Co, Ni–P, Co–P, Ni–Co–P, Ni–W, Ni–Mo and so on, and many coating techniques are available, involving CVD, laser cladding and thermal spraying. Among these systems, Ni–Co, Ni–P and Co–P coatings have attracted considerable attention at industrial scale due to their excellent mechanical properties, corrosion resistance and special magnetic characteristics [31]. First, the deposition and thermal spraying of single Ni or Co metal have been in detail described in some classical literature and reviews [32, 33], and this is also considered as an initial Cr replacement coating in industrial fields. Afterward, the superior corrosion and tribological performance of the Ni–Co compared to single Ni were found, and thus, Ni–Co metal coating was extensively applied in spite of the higher price of Co [34]. An in-detail review of Ni–Co metal coatings including electrodeposition mechanism, key operational parameters, chemical compositions, microstructure, thermal stability, performances and applications has been summarized by Karimzadeh et al. [35], which holds promise for providing ideas for the further development of Ni–Co-based coatings. It is important to be aware of the continuous increase in Co/Ni price, and thus, the incorporation of P as an alloying element in Ni/Co coatings has been developed and considered as a potential Cr alternative owing to possessing desirable properties. Continuously, detailed research and industrial-scale application have shown an excellent corrosion resistance of the Ni–P and Co–P alloy coatings at a wide range of environment conditions [36–45]. In recent years, Luo et al. [36–39] explored the growth mechanism of the Ni–P coating and its corrosion behavior under harsh service environments, like the coexistence of O_2, CO_2 and H_2S, and the results suggested that a uniform amorphous microstructure with enhanced corrosion resistance of the coatings can be well achieved with increasing P content. Accordingly, a large number of preparation techniques of Ni–P coatings on steel surfaces have also been developed [37, 38, 40]. A key

Table 1 A summary comparing preparation, performance and applications of Ni–P/Co–P coatings based on latest studies [36–45]

Type	Preparation	Performance	Application	References
Ni–P	25 g/L $NiSO_4{\cdot}6H_2O$, 30 g/L $NaH_2PO_2{\cdot}H_2O$	$R_{0.01\ Hz}$ = 3086 Ω cm^2 at 43 h immersion	Electronics industry	[36]
	pH: 5.5–6.0, 90 °C		Oil and gas industry	
	25 g/L $NiSO_4{\cdot}6H_2O$, 30 g/L $NaH_2PO_2{\cdot}H_2O$	Corrosion rate of 0.0036 mm/a in CO_2 solution at 168 h		[38]
	pH: 5.5–6.0, 85 °C			
	20 g/L $NiSO_4{\cdot}6H_2O$, 25 g/L $NaH_2PO_2{\cdot}H_2O$	i_{peak} of Ni–P coating in 3.5 wt.% NaCl solution at 0.1 V_{SCE} is higher than that of 304SS steel in tap water at 0.2 V_{SCE}		[39]
	pH: 5.5–6.0, 85 °C			
Ni–P–Re	0.100 mol/L $NiSO_4{\cdot}7H_2O$, 0.001–0.0075 mol/L NH_4ReO_4, 0.200 mol/L $NaH_2PO_2{\cdot}H_2O$	Rhenium can improve thermal stability of Ni–P coatings	–	[40]
	pH: 3.5–6.0, 85–90 °C			
Ni–P–nano-ZrO_2	15 g/L $NiSO_4{\cdot}6H_2O$, 25 g/L $NaH_2PO_2{\cdot}H_2O$, 5 g/L ZrO_2 nanoparticles	I_{corr} decreased evidently to 7.135 × 10^{-6} A cm^{-2}	Ceramic	[37]
	pH: 5.0–5.5, 85 °C			
Co–P	15 g/L $CoSO_4{\cdot}7H_2O$, (2, 5, 10) g/L NaH_2PO_2	Average microhardness values of heat-treated deposited Co–P coatings increased to 940 HK	Aviation and automotive industries	[41]
	150 mL/L cobalt sulphamate, 20 mL/L H_3PO_4, 0–10 g/L NaH_2PO_2	R_{ct} value increased to 11 kΩ cm^2 with increasing P content		[42]
	0.084 mol L^{-1} $CoCl_2{\cdot}6H_2O$, 0.222 mol L^{-1} $NaH_2PO_2{\cdot}H_2O$, 25 °C	A better electrocatalytic performance with a current density of 40 mA cm^{-2}		[43]
	180 g/L $CoCl_2{\cdot}6H_2O$, 4.4 g/L $CoCO_3$, 2.17 cm^3/L H_3PO_4, 15 g/L H_3PO_3,	Wear resistance increasing with increasing P content		[44]
	pH: 1.0, 80 °C			
Co–P–MoS_2	155 g/L $CoSO_4{\cdot}7H_2O$, 30 g/L $CoCl_2{\cdot}6H_2O$,	Co–P–10 g/L MoS_2 film obtained at 25 A dm^{-2} exhibited most favorable tribomechanical performance	–	[45]
	12 g/L $Na_2H_2PO_2$, pH: 2.0, 80 °C			

$R_{0.01\ Hz}$—Impedance at 0.01 Hz; i_{peak}—peak current; I_{corr}—corrosion current; R_{ct}—charge transfer resistance

issue is that an increase in brittleness for the Ni–P coatings gradually appears during the heat treatment at a higher P content, especially under a harsh wear condition. On the other hand, the review proposed by Bera et al. [41] provides a critical overview on the advances and fundamental considerations of Co–P metal coatings as well as addressing the influence of various operating parameters. A summary comparing the performances and applications of Ni–P/Co–P coatings based on the latest studies [36–45] is provided in Table 1.

Despite the favorable engineering benefits of Ni–P and Co–P coatings, the high costs of Co/Ni metals and phosphorus as a potential water contaminant should be carefully considered, in which the electroplating process of Co/Ni metals and phosphorus produces hazardous wastewater, giving rise to a threat to environment and human health. In comparison, the metal coatings prepared by thermal spraying have a series of advantages, e.g., the simplification of preparation process, conservation of resources, low levels of pollution, and so on, which continuously evolve to meet new challenges arising from the electroplating process [46], involving high-velocity oxygen fuel spray (HVOF) [47–49], plasma spray [50, 51], arc spray [52] and cold spray. A large number of Fe-based amorphous coatings with excellent wear/corrosion have been prepared by thermal spray techniques (e.g., preparing $Fe_{60}Cr_8Nb_8B_{24}$ amorphous coating using HVOF proposed by Koga et al. [47], Fe–40Al metallic alloy coating using HVOF proposed by Ji et al. [48], Fe–Cr–Nb–B coating using HVOF proposed by Guo et al. [49], $Fe_{62}Ni_3Cr_4Mo_2W_3Si_6B_{17}C_3$ amorphous coating using plasma spray proposed by Liu et al. [50], $Fe_{48}Cr_{15}Mo_{14}C_{15}B_6Y_2$ amorphous metallic coatings using plasma spray proposed by Zhou et al. [51], FeBSiCrNbMnY amorphous/nanocrystalline metallic coating using arc spray proposed by Lin et al. [52], FeCrNiNbBSiW amorphous coatings using high-velocity spray by Zhang et al. [53], etc.), in which the plasma spray exhibits higher efficiency and possesses a broader application potential owing to its superior adhesive strength and compact structure compared to HVOF spray, and arc spray possesses a high efficiency at a large-area preparation though the work in this regard is scarce. In addition, the preparation and performance of Fe-based amorphous coatings based on the latest reports [47–58] are summarized in Table 2.

In addition, high-entropy alloy coatings have also attracted considerable attention at industrial scale in recent years, and a summary comparing the performances and applications of high-entropy alloy coatings based on the latest studies [59–73] is provided in Table 3.

2.2 Metal–nanoparticles composite coatings

The favorable properties (mechanical, tribological and electrochemical characteristics) of metallic coatings can be further enhanced by the appropriate second phase or other nanoparticles being well dispersed throughout the matrix, which further expands their application under various conditions, and these benefits depend on their content, degree of dispersion, material type and shape. Currently, the most commonly used nanoparticles include aluminum oxide (Al_2O_3) [74–77], silicon carbide (SiC) [78, 79], silicon dioxide (SiO_2) [80, 81], titanium dioxide (TiO_2) [82, 83], titanium nitride (TiN) [84], molybdenum disulfide (MoS_2) [85, 86], etc. For instance, silane incorporation in the metallic coating is an effective method, in which the silane molecules were crosslinked with each other by Si–O–Si bond and the film was bound to the metal surface through Si–O–metal bonds, and thus, silane incorporation was considered as an effective substitute for the traditional environment-unfriendly methods of chromate passivation and phosphate coatings. In addition, Wang et al. [80] found that the incorporation of SiO_2 nano-particulates into the Ni–W alloy matrix significantly increased its corrosion resistance since the SiO_2 nano-particulates can effectively weaken the corrosion process by filling in crevices, gaps and microscopic holes on the surface of the Ni–W alloy. Unfortunately, the major drawbacks of low thickness and high concentration of defects of the coatings would significantly destroy their anti-corrosion efficiency. An optimum content (12.5 mL L^{-1}) of TiO_2 dispersed in the Co metallic coating was reported in the work of Wang et al. [80], and a superior corrosion and tribomechanical performance were achieved on the basis of good surface smoothness [82]. In other words, too much or too little contents of TiO_2 nanoparticles are both associated with inevitably accelerating the corrosion behavior, and thus, this coating is still at the laboratory level. Similarly, the addition of MoS_2, a layered solid lubricant, with appropriate concentration was favorable to the increase in compactness of the metallic coating according to the Orowan mechanism [85, 86]. In the work of Wang et al. [67], the metallic coating prepared by co-evaporation of MoS_2 and Co was characterized by an excellent adhesion and improved friction coefficient. In addition, Al_2O_3@MoS_2 composited with metal Ni was deposited on the surface of steel, as summarized by Huang and Xiong [77], and the results showed that the corrosion resistance of the composite coating is the strongest when Al_2O_3 is 50 wt.%, which can be explained by Al_2O_3@MoS_2 acting as an inert physical barrier to prevent the formation and development of corrosion sites. On the other hand, an obvious improvement of the microstructures and properties for $Fe_{50}Mn_{30}Co_{10}Cr_{10}$ high-entropy alloy can be achieved via the addition of NbC nanoparticles and using

Table 2 Preparation process and performance of representative Fe-based amorphous coatings [47–58]

Type	Preparation	Corrosion performance	Mechanical performance	References
$Fe_{60}Cr_8Nb_8B_{24}$	HVOF, powder size range: 20–53 μm, oxygen flow: 896.8 L/min, kerosene flow: 22.1 L h^{-1}, O_2/kerosene equivalence ratio: 1.3, step size: 10 mm	–	Porosity: 5.7 ± 0.6%, *Ra*: 8.2 ± 0.2 μm, Hardness: 838 ± 23 $HV_{0.3}$	[47]
Fe–40Al	HVOF, nozzle length: 76 mm, nozzle diameter: 8 mm, oxygen flow rate: 400 L/min, natural gas: 180 L/min, carrier air gas: 30 L/min, stand-off distance: 280 mm, powder feed rate: 28 g/min	Powder size (60 μm): E_p = 50 mV_{SCE}, Powder size (50 μm): E_p = 95 mV_{SCE}, Powder size (30 μm): E_p = 100 mV_{SCE}	Powder size (60 μm): hardness (HV 300) = 349 ± 37, Powder size (50 μm): hardness (HV 300) = 395 ± 39, Powder size (30 μm): hardness (HV 300) = 307 ± 28	[48]
Fe–Cr–Nb–B	HVOF, powder size range: 20–53 μm, oxygen flow: 897 L/min, kerosene flow: 22.3 L/h, oxygen/kerosene ratio: 1.3	–	Hardness: 890 ± 75 HV	[49]
$Fe_{62}Ni_3Cr_4Mo_2W_3Si_6B_{17}C_3$	LPPS, arc current: 600 A, argon flow rate: 50 L min^{-1}, spraying distance: 350 mm, gun traverse speed: 150 mm s^{-1}, powder feed rate: 30 g min^{-1}, hydrogen flow rate: 4, 6 and 8 L min^{-1}	A passive current density of about 4 A m^{-2} in 1 mol/L HCl solution	Lowest porosity of about 0.04% is obtained at 8 L min^{-1} hydrogen flow rate	[50]
$Fe_{48}Cr_{15}Mo_{14}C_{15}B_6Y_2$	SPS, H_2: 5.0 L/min, powder feed rate: 6.0 g/min, spray distance: 110 mm, Ar: 100–120 L/min, power: 54–62 kW	–	Amorphous content and microhardness can reach 96.78% and 1005 $HV_{0.1}$, whereas porosity is only 0.85% at spraying power of 62 kW and Ar flow rate of 110 L/min	[51]
FeCrNiNbBSiW and FeCrNiNbBSiMo	Voltage: 36 V, current: 160 A, wire feed rate: 27 m/min, air-jet pressure: 0.7 MPa, spray distance: 200 mm, moving speed: 1.6 m/min	–	High bonding strength (≥ 42 MPa) and low porosity (≤ 3.5%)	[53]
$Fe_{40}Cu_8Cr_{15}Mo_{14}C_{15}B_6Y_2$	AC-HVAF, spraying distance: 330, 180, 280, 180 mm, air pressure (In Pa): 103–123, 118–123, 110–128, 110–126, fuel pressure (In, Pa):127–139, 91–99, 83–87, 82–85, air pressure (Out, Pa): 90.9–91.8, 91.0–91.7, 84.4–91.4, 85.0–92.0, fuel pressure (Out, Pa): 76.4–76.6, 76.2–76.4, 76.5–78.8, 76.4–78.7	–	Average hardness is 13 $HV_{0.1}$	[54]
Fe-$W_{10}Cr_4Ni_3Mo_2B_4Si_4C_1$	Atmospheric plasma spraying, voltage: 50, 60, 70 and 80 V, power: 25, 30, 35 and 40 kW, the other shown as Ref. [52]	–	Lowest porosity reached 2.6	[55]
$Fe_{54.2}Cr_{18.3}Mo_{13.7}Mn_{2.0}W_{6.0}B_{3.3}C_{1.1}Si_{1.4}$	AC-HVAF AMC, particle size ≤ 0.045 mm, spray distance: 180 mm, powder feeding rate: 3 g min^{-1}, turntable rate: 133 r min^{-1}, reciprocal time: 10 cycle, air pressure: 82 Pa, fuel pressure: 70 Pa	AC-HVAF AMC exhibited a lower passive current density and pitting resistance than that of HVOF AMC	Porosities of AC-HVAF and HVOF AMCs were 1.03% and 1.25%. Amorphous phase content and microhardness of AC-HVAF AMC were both higher than those of HVOF AMC	[56]
FeMoCrCoYCSiAlO	APS, powder size: 12, 29 and 56 μm, spray powers: 15, 22.5 and 30 kW, arc currents: 300, 450 and 600 A, arc voltage: 50 V, argon flow rate: 3000 L/h, hydrogen flow rate: 80 L/h, spray distance: 100 mm, gun pass speed: 350 mm/min	–	Runs 1: 1099 ± 100 $HV_{0.1}$ Runs 2: 1011 ± 45 $HV_{0.1}$ Runs 3: 884 ± 61 $HV_{0.1}$	[57]
FeCrBSiNbW	Arc spraying process, spraying voltage: 36 V, wire feed rate: 2.7 m/min, compressed air pressure: 700 kPa, stand-off distance: 200 mm, gun traverse speed: 100 mm/s	–	Wear resistance of FeCrBSiNbW coating is about 4.6 times higher than that of 3Cr13 coating under same testing condition. In 3.5% NaCl aqueous solution, coating has better corrosion resistance than that of 0Cr18Ni9 stainless steel coating	[58]

Ra—High average surface roughness; E_p—passivation potential; LPPS—low pressure plasma spraying; SPS—supersonic plasma spraying; AC-HVAF—activated combustion-high velocity air fuel; AMC—amorphous metallic coating; APS—air plasma spraying

Table 3 Preparation process and performance of representative high-entropy alloy coatings [59–73]

High-entropy alloy (HEA) coating	Preparation method	Process parameter	Corrosive media	Performance	References
AlCoCrFeNi	Gas tungsten arc (GTA) cladding	Cladding current: 150–230 A, powder thickness: 1.5–2.5 mm, traveling speed: 1.75 mm/s, Ar flow rate: 15 L/min, arc gap: 4 mm, electrode type: W–2 wt.% CeO_2, electrode shape: ϕ2.4 mm, 45°	3.5 wt.% NaCl	S-150 (E_{corr} = − 654 mV_{SCE} I_{corr} = 11.86 μA cm^{-2}), S-180 (E_{corr} = − 515.83 mV_{SCE}, I_{corr} = 10.86 μA cm^{-2})	[59]
AlCrFeMoTi	Magnetron sputtering	Base pressure: 2 × 10^{-3} Pa, Ar flow rate: 52 cm^3/min, working pressure: 0.53 Pa, working temperature: 300 °C, substrate bias voltage: – 100 V, sputtering power: 200 W, deposition time: 2 h	LBE	As-deposited AlCrFeMoTi coating displayed high hardness (8.32 GPa) and excellent corrosion resistance against LBE	[60]
$Al_{0.4}CoCu_{0.6}NiSi_{0.2}Ti_{0.25}$	Laser cladding	Particle sizes: 20 ± 5 μm, laser power: 150 W, laser conversion angle: 75°, thickness of coating: 120 μm	4 wt.% NaCl	HEA coating (E_{corr} = − 0.506 V_{SCE}, I_{corr} = 2.14 × 10^{-5} A cm^{-2})	[61]
AlCoCrFeNi	Arc cladding	Cladding currents: 180 A, arc voltage: 15 V, speed: 1.5 mm/s, shielding gas flow rate: 15 L/min	3.5 wt.% NaCl	E_{corr} = − 241.5 mV_{SCE}, I_{corr} = 0.132 μA cm^{-2}	[62]
AlCoCrCuNiTi	Laser cladding	Power: 2000 W, laser spot diameter: 3 mm, cladding speed: 30 mm/s, overlapping rate: 35%	–	Maximum microhardness of TiN/AlCoCrFeNiTi HEA coating is about 737 HV	[63]
AlCrTiNbMo	Electron beam cladding	High voltage: 55 kV, beam current: 10 mA, focus current: 2500 mA, scanning frequency: 200 Hz, scanning amplitude: V_x = V_y = 17, vacuum degree: 5 × 10^{-2} Pa	–	Mass loss (35 min test): Ti600 (38.81 mg), HEA coating: (1.02 mg)	[64]
$Al_xCoCrFeNiTi_{1-x}$	Laser cladding	Laser power: 2.0 kW, scanning speed: 11 mm/s, spot diameter: 4 mm, powder mass flow: 6 g/min, lapping rate: 50%	3.5 wt.% NaCl	E_{corr} = − 573.847 mV_{SCE}, I_{corr} = 10.05 nA cm^{-2}	[65]
AlCoCrFeNi	Thermal spray	Voltage: 65 V, primary gas flow, Ar: 42.1 L/min, secondary gas flow, H_2: 2.35 L/min, powder feed rate: 17–21 g/min, powder carrier gas flow, Ar: 6 L/min, stand-off distance: 90 mm	Filtered sea water	AlCoCrFeNi (E_{corr} = − 321 mV_{SCE}, I_{corr} = 0.83 μA cm^{-2})	[66]
$CoCrFeNiCu_{1-x}Mo_x$	Coaxial direct laser deposition	Laser powder: 1100 W, laser spot size: 3 mm, scanning velocity: 350 mm/min, powder flow rate: 16 g/min, carrier gas flow: 7 L/min, shielding gas flow: 35 L/min, overlapping ratio: 40%	3.5 wt.% NaCl	$Cu_{0.25}Mo_{0.75}$ (E_{corr} = − 0.010 V_{SCE}, I_{corr} = 4.273 × 10^{-6} A cm^{-2})	[67]
CoCrFeNi	Laser cladding	Laser power: 400 W, scanning speed: 5 mm/s, Ar atmosphere	3.5 wt.% NaCl	1000 °C-annealed CoCrFeNi coating showed a pronounced passive platform (E_{corr} = − 0.168 V_{SCE})	[68]
$CoCrFeNiAl_xMn_{1-x}$	Laser cladding	Laser spot diameter: 3 mm, scanning speed: 4 mm/s, overlapping rate: 40%, powder flow rate: 3.3 g/min, laser power: 1300 W	3.5 wt.% NaCl	$CoCrFeNiAl_{0.8}Mn_{0.2}$ coating (impedance: 25,016.228 Ω/cm^2, Corrosion rate: 0.0464 g/(m^2 h))	[69]
$CoCrFeNiCu_{1-x}Mo_x$	Coaxial direct laser deposition	Spot diameter: 3 mm, laser power: 1100 W, scanning rate: 350 mm/min, overlapping rate: 4%, powder flow rate: 16 g/min, carrier gas flow rate: 7 L/min, shielding gas flow rate: 35 L/min	0.5 mol/L H_2SO_4	$Cu_{0.25}Mo_{0.75}$ (E_{corr} = − 0.272 V_{SCE}, I_{corr} = 3.954 × 10^{-6} A cm^{-2})	[70]
CoCrFeNiTiMo	Double cathode glow discharge	Base pressure: 5 × 10^{-4} Pa, gas pressure: 35 Pa, double cathode glow discharge deposition voltage: − 900 V, bias voltage: − 300 V	3.5 wt.% NaCl	E_{corr} = − 0.348 V_{SCE}, I_{corr} = 9.82 × 10^{-7} A cm^{-2}	[71]
NiCoCrAlSi	Plasma spark sintering	Process temperature: 1170 °C, soaking time: 15 min, aluminum intermediate layer: 20 μm, applied pressure: 30 MPa	90 wt.% Na_2SO_4, 10 wt.% NaCl	HEA-15F (n = 0.33, K_p = 6.52 × 10^{-5} mg^2 cm^{-4} s^{-1}, R^2 = 0.99)	[72]
$CoCr_2FeNiMo_{0.3}$	Laser cladding	Spot diameter: 1 mm, laser power: 700 W, scanning rate: 450 mm/min, overlapping ratio: 40%	3.5 wt.% NaCl	$CoCr_2FeNiMo_{0.3}$ (E_{corr} = –272 mV, I_{corr} = 39 μA cm^{-2})	[73]

E_{corr}—Corrosion potential; K_p—parabolic constant rate; R^2—goodness of fit; LBE—Lead-Bismuth eutectic

Table 4 Preparation process and performance of representative particle-reinforced metal–nanoparticles composite coatings [74–88]

Metal–nanoparticle	Preparation method	Process parameter	Corrosive media	Performance	References
Ni–W–Al_2O_3	Electrochemical deposition	pH: 6 ± 0.15, 30 °C, average current density: 3 A dm^{-2}, agitation rate: 190 ± 10 r/min	3.5 wt.% NaCl	Coefficient of friction for sliding distance decreases to 4.5 ± 0.5 and coefficient of friction of Ni–P–MoS_2 composite coating on bearing steel balls decreases to 0.05	[74]
Al_2O_3	Atomic layer deposition	pH: 7.2 ± 0.2, 160 °C, deposition rate: 0.048 nm/cycle	0.2 mol/L NaCl	Average dissolution rate of alumina coating in neutral 0.2 mol/L NaCl is approximately 7 nm h^{-1}	[75]
Al_2O_3	Anodized samples	Constant voltage: 28 V at 283 K, constant current density: 100 A m^{-2}, room temperature dry: 25.92 Ms	3.5 wt.% NaCl	Both anodic and cathodic currents are further decreased to less than 10^{-8} A cm^{-2} after desiccation treatment	[76]
MoS_2/Al_2O_3	Pulse electrodeposition	pH: 6, 50 ± 2 °C, peak current density: 1.5 A cm^{-2} duty cycle: 2/3	0.5 mol/L NaCl	Ni–MoS_2/50 wt.% Al_2O_3 coating has lowest current density of 26.3 μA cm^{-2}	[77]
Ni–W–SiC	Electrodeposition	pH: 2.5, 60 °C, current density: 6 to 18 A dm^{-2}, stirring rate: 60–240 r/min	0.5 mol/L NaCl	2.36% SiC has wide passive region and smaller passive current density as well as microhardness variation of 711 Hv	[78]
Ni–W–SiC	Pulsed electrodeposition	pH: 9, 60 ± 2 °C, current density: 48 mA cm^{-2}	–	Hardness of heat-treated Ni–W/SiC increases and grain size decreases from 7 to 3.8 nm	[79]
Ni–W–SiO_2	Direct current deposition electroplating	pH: 7.5, 60 °C, current density: 4 A dm^{-2}	3.5 wt.% NaCl	Lowest current density was 26.3. Highest hardness value reached 823 HV	[80]
Ni–W–SiO_2	Pulsed electrodeposition	pH: 3, 25 ± 2 °C, pulsed parameter: –15 mA cm^{-2}	3 wt.% NaCl	Nanocomposite electroplated at pH 4 is smoother, thicker, more compact, more homogenous and harder when compared to film obtained at pH 3	[81]
Co–TiO_2	Electrodeposition	pH: 4.2, 40 ± 1 °C, 60 g/L TiO_2 in bath, 30 mA cm^{-2} and 0.15 g/L SDS ($C_{12}H_{25}SO_4Na$)	3.5 wt.% NaCl	Hardness of Co–TiO_2 nanocomposite increased to 504 HV. Lowest current density was 1.913 μm/cm^2	[82]
Ni–Co–TiN	Pulse current electrodeposition	pH: 4.2 ± 0.2, 50 °C, current density: 2–8 A dm^{-2}	3.5 wt.% NaCl	For ultrasonic-assisted coatings, optimum current density is 6 A dm^{-2}, with a tighter structure and better corrosion resistance	[84]
Ti–MoS_2	Thermal deposition	Pulse rate: 0.033 s^{-1}, evaporation rate: 1 nm s^{-1}	–	Ti + IF (inorganic fullerene-like) film were thoroughly characterized and tribological measurements showed significant reduction in both friction and wear, compared with a pure titanium film	[85]
Co–MoS_2	Electrodeposition	60 °C, low current density: 2.5 A cm^{-2}	–	Coefficient of friction of Ni–P–MoS_2 composite coating on bearing steel balls decreased from 0.45 to 0.05 compared to pure Ni–P coating	[86]
NbC	Laser cladding	Laser power: 2500 W, spot size: 4 mm, scanning speed: 3 mm/s, overlapping rate: 30%, argon shielding gas	–	Average Vickers hardness and friction coefficient value were 525 HV and 0.45 separately	[87]
Al_2O_3–13 wt.% TiO_2	Plasma spraying	Power: 45 kW, main gas flow (L/min) Ar:H_2 = 70:7, carrier gas flow: 12 L/min, powder feed rate: 30 g/min	–	Wear resistance of composite coatings was increased by about 1.3–4.9 times	[88]

laser cladding technique, with the average Vickers hardness and friction coefficient value being 525 HV and 0.45 respectively [87]. Similarly, Al_2O_3–TiO_2-reinforced CoCrFeMnNi high-entropy coatings were prepared by the plasma spraying technique, and the wear resistance of the composite coatings was increased by about 1.3–4.9 times [88]. However, it is important to find the appropriate content and control the distribution beneath the coating subsurface. Moreover, the most favorable properties of these particle-reinforced metal–nanoparticles composite coatings are outlined in Table 4 [74–88].

2.3 Metal–ceramic composite coatings

These metal coatings on the surface of low alloy steel can not only protect the metal substrate from corrosion, but also have the advantage of beautifying the appearance of decorative materials, which is favorable to further improve their industrial application ranges. However, some obstacles of metallic coatings, involving high porosity, oxidizable characteristic and internal cracks, still exist and need to be solved. On the other hand, the multifunctional requirements of metal coatings cannot be simultaneously met based on its relatively single characteristic. Thus, the

development of multifunctional coatings like excellent wear/corrosion resistance and enhanced hardness will be the central issue in the future. Currently, the metal–ceramic composite coatings prepared by adding cermet materials into the metal coatings to achieve multifunction have been a research hotspot in the related fields. Among them, the WC–Co coatings have been maturely applied in the industrial production, and the bonding phase of WC–Co coatings is η phase (Co_3W_3C and Co_6W_6C), which can effectively enhance the corrosion resistance of the coatings, while this issue has received enough interests in a significant body of scientific research [89–91].

In 1990s, laser-cladded ceramic–metal composite coatings with various compositions were developed and the performance was strongly dependent on the content, size and distribution of ceramic particles [89–94]. Pei et al. [89] studied the performance of the WC–Co metal–ceramic composite coating and found that the adhesion between the coating and the substrate was insufficient. In addition, some issues involving the occurrence of over-burning and/or residual thermal stress during the spraying process are not negligible. Meanwhile, Tani et al. [90] also identified that adhesion is a critical factor affecting the performance of WC–Co coatings, especially in the corrosion/wear resistance of WC–Co coatings. In this regard, Bao et al. [91] used a supersonic flame spraying technique to prepare a WC–Co coating on the surface of the steel and the results indicated that no obvious decomposition or loss was observed in the cross-sectional morphology of the coatings, accompanied by the decreased porosity and enhanced interfacial adhesion. Wang et al. [92] specially designed/modified the WC–Co coating and prepared a new WC–Co_2Cr_3 coating by adding a small amount of Cr element into Co, WC and W_2C phases in the WC–Co_2Cr_3 coating, as shown in Fig. 2, in which the dissolution of Cr in the carbides was in favor of significantly reducing the potential difference between the carbides and the metal binding agent in the WC–Co_2Cr_3 coating and effectively improved the resistance of the coating to micro-galvanic corrosion compared to the traditional WC-based coatings.

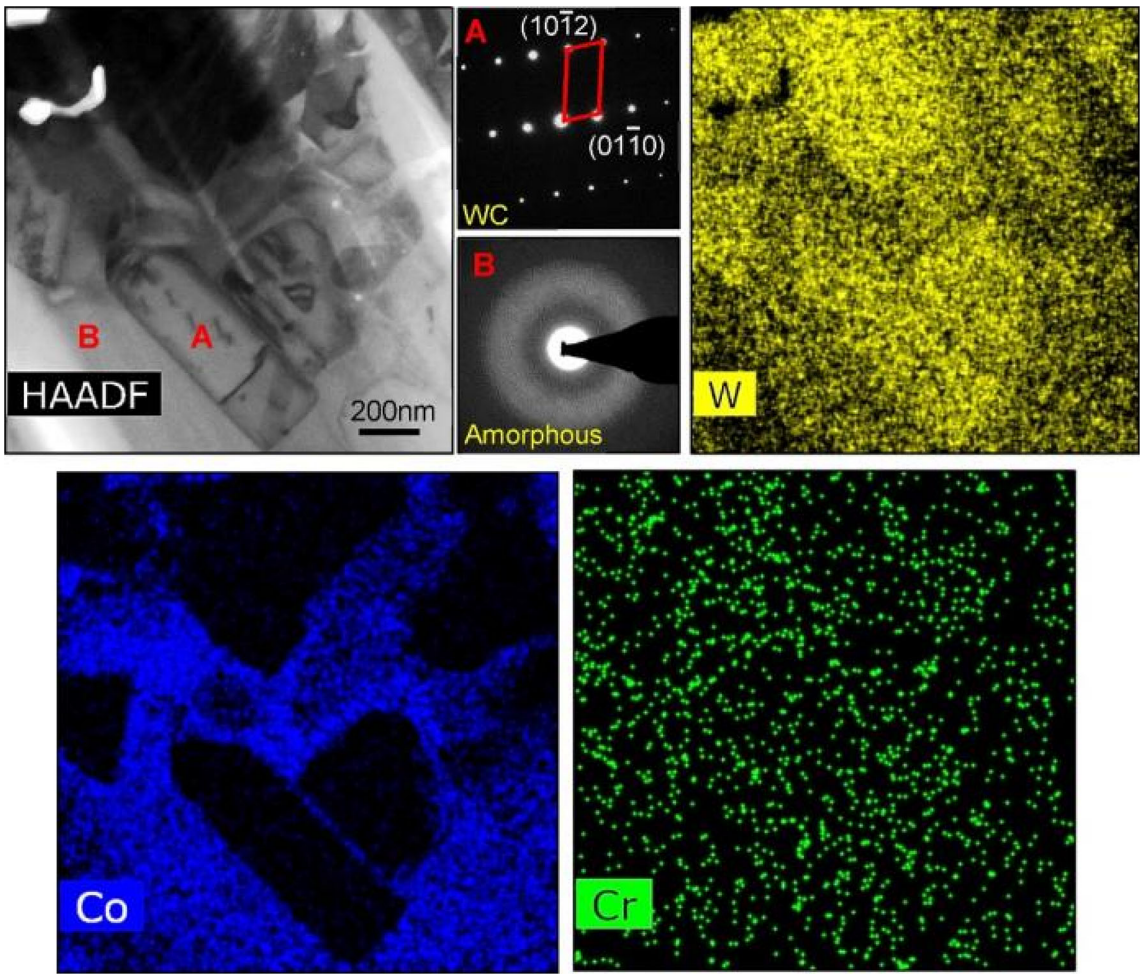

Fig. 2 High-angle annular dark field (HAADF) scanning transmission electron microscopy image of WC–Co_2Cr_3 coating, with selected area electron diffraction patterns of marked areas and corresponding element mapping for W, Co and Cr [92]

Recently, systematic numerical simulations have been applied to investigate the first-layer deposition efficiency of ceramic on metal substrates, providing new mechanistic information for understanding the initial stage of composite coatings, and an optimum grain size range was proposed for lower fragmentation and higher retention [93, 94]. In comparison, a series of ceramic particles, such as TiC [95–98], TiN [99–102], Al_2O_3 [101–104] and WC [105, 106], can be used to improve the mechanical and corrosion properties of high-entropy alloy coatings. And the preparation and most favorable properties of these ceramic particle-reinforced coatings are summarized in Table 5. Despite the existence of many benefits, the fragmentation of ceramic phases is still a puzzling problem to be solved in future research.

3 Diffusion coatings

Some coating materials and technologies may be considered for the improvement of integrity of the steel surface in high-temperature environments since many coating options are not suitable for application under high temperatures. Diffusion coatings refer to diffusing some elements into the substrate to form a new surface with specific functions [107], which are currently one of the most suitable coatings at high temperatures. The common diffusion coatings are mainly obtained by powder plating, CVD, PVD, ion implantation and other methods. Among them, the powder plating is a relatively traditional coating preparation technology, which can improve the corrosion resistance of the steel by changing the structure and composition of the material surface. The obtained coating has a uniform thickness and a strong bond with the substrate, but requires a higher operating temperature [108]. Additionally, the applications of PVD and CVD techniques have mainly concentrated on the industrial preparation of diffusion coatings [109–111]. The thin film with special properties generated by PVD has strong adhesion and dense structure; however, its application remains limited due to the disadvantages of limited deposition rates, single direction and uncontrollable compositions. In comparison, these limitations can be compensated by CVD technology considering its advantages of multi-directional/accelerated depositions with high purity. In this process, the diffused metal and gas phase reactant undergo a chemical reaction to form a volatile metal compound, and then, the compound is decomposed, deposited and diffused into the metal matrix to form a diffusion coating at a higher temperature. The parameters, mechanism and electrochemical characteristics of diffusion coatings prepared by PVD and CVD technologies have also received enough interests in recent years.

The effective improvement of corrosion resistance of steel has been experimentally determined via the involvement of a small number of carbides, like vanadium and niobium, into Cr diffusion coating. In a recent study, OrjuelaG et al. [112] integrated the advantages of both PVD and CVD surface treatments and deposited a niobium carbide (NbC) diffusion coating on AISI-1045 low alloy steel, through which the enhanced corrosion resistance of the substrate was well achieved, whereas the characteristics of porosity and poor adhesion of the coating–substrate interface restricted the long-term protection of coatings (Fig. 3).

In order to further reduce the porosity of diffusion coatings, Liu et al. [113] used the PVD technology to prepare a compact CrN coating with fine equiaxed grains, and its porosity was significantly reduced, thereby restricting the diffusion of the corrosive medium to the coating/steel interface. Dobruchowska et al. [114] prepared Al–Mn–Si diffusion coating on AISI-4140 alloy steel substrate by the CVD method, and the obtained coating was characterized by the excellent corrosion resistance, stable passivation ranges, along with enhanced re-passivation ability. In addition, the enhancement of corrosion resistance provided the possibility for practical application of the coatings in the chloride-rich environment since no obvious corrosion rusts were observed on the coating surface after the salt spray test lasted for 1000 h, as described in Fig. 4.

According to the review above, it can be concluded that PVD and CVD techniques can provide good adhesion of the coatings to metallic substrates and may be of high potential when appropriate coating compositions are selected, in which the CVD is more applicable for the material with various shapes compared to that of PVD. Although the industrialization degree of these coatings has been very mature, the literature research for technological improvement is relatively less under the consideration of the high operation cost of PVD and CVD coating technologies and limitation of diffusion coating composition. (No chromium or low chromium makes it difficult to further decrease the porosity of the coating.) Thus, PVD and CVD technologies presently focus on depositing diffusion coating on stainless steel surface to enhance its corrosion resistance and exploring its application in many precision instruments and extreme environments. The preparation and performance of diffusion coatings according to the latest literature [109–120] are followed as Table 6.

On the other hand, it is important to be aware that transition layers are usually indispensable for improving the adhesion property and service performance of the metal and diffusion coatings on steel. Continuously, a large number of detailed research regarding their preparation techniques and mechanism of the enhanced adhesion and

Table 5 Preparation process and performance of representative HEA–ceramic composite coatings [95–106]

Type	Ceramic particle	Preparation	Process parameter	Performance	References
FeMnCrNiCo	TiC	Laser cladding	Laser beam spot diameter: 3 mm, scanning velocity: 6 mm/s, flow rate: 25 mL/min	FeMnCrNiCo + 10 wt.% TiC coatings exhibited an excellent anti-wear property, with a variance of friction coefficient is 0.01109	[95]
FeCoCrAlNiTi	TiC	Laser surface alloying	Laser power: 2000 W, scanning speed: 0.3 m/min, spot diameter: 3 mm, overlapping ratio: 50%, Ar shielding gas	Specific wear rate of 30TiC sample was 2.636×10^{-5} compared to 2.437×10^{-4} $mm^3/(N\ m)$ for FeCoCrAlNiTi sample	[96]
CrMnFeCoNi	TiC	Laser cladding	Spot diameter: 3 mm, scanning velocity: 6 mm/s, powder feeding speed: 2.5 r/min, argon shielding gas flow rate: 3.5 L/min, overlapping ratio: 30%	T20C coating exhibited high hardness (362.5 $HV_{0.3}$), low wear rate (0.16242) due to formation of composite oxide film on worn surface	[97]
CoCrFeMnNi	TiC	Laser cladding	Laser power: 1300 W, scanning velocity: 6 mm/s, Ar shielding gas flow rate: 25 mL/min, overlapping ratio: 30%	Under large compression deformation, internal cracks in heterogeneous coating (HC) can be effectively reduced compared with composite coating (CC) owing to good plasticity of CoCrFeMnNi transition layer	[98]
AlCoCrFeNi	TiN	Plasma spray	Laser power: 2000 W, laser beam spot diameter: 5 mm, laser scanning velocity: 7 mm/s	As-remelted AlCoCrFeNi(TiN) coating exhibited highest microhardness value of 851 $HV_{0.3,}$ which was attributed to formation of in-situ Al_2O_3 + TiN and nano-particles dispersion strengthening	[99]
FeCoNiCrMnTi	TiN	Laser cladding	Laser power: 2000 W, laser beam radius: 2.5 mm, scanning speed: 10 mm/s, coaxial powder feeding rate: 12 g/min, overlapping ratio: 30%	Substrate (E_{corr} = − 0.217 V, $I_{corr} = 5.45 \times 10^{-6}$ mA cm^{-2}), Ti_0 (E_{corr} = − 0.161 V, $I_{corr} = 3.37 \times 10^{-6}$ mA cm^{-2}), $Ti_{0.5}$ (E_{corr} = − 0.209 V, $I_{corr} = 1.15 \times 10^{-7}$ mA cm^{-2}), Ti_1 (E_{corr} = − 0.247 V, $I_{corr} = 3.18 \times 10^{-7}$ mA cm^{-2}), $Ti_{1.5}$ (E_{corr} = − 0.412 V, $I_{corr} = 3.96 \times 10^{-5}$ mA cm^{-2}). While atomic ratio of Ti in $FeCoNiCrMnTi_x$ exceeded 1.0, corrosion resistance of coatings decreased	[100]
CoCrFeNiMn	TiN–Al_2O_3	Plasma cladding	Current: 170 A, scanning velocity: 100 mm/s, powder feeding rate: 7 g/min	Wear volume of H1 coating (TiN–Al_2O_3 reinforced) was 1.07×10^{-3} mm^3, which reduced by 12.5% compared to pure HEA coating	[101]
CoCrFeMnNi	TiN–Al_2O_3–Cr_2B	Plasma cladding	Working current: 230 A, scanning speed: 110 mm/min, swing speed: 1300 mm/min, centered Ar gas flow: 1.7 L/min, working Ar gas flow: 3 L/min, protective Ar gas flow: 9 L/min, powder feed rate: 15 g/min	Wear rate at different temperatures was reduced to 20.48% (room temperature), 34.75% (200 °C), 16.13% (400 °C) and 10.12% (600 °C) compared to pure HEA coatings	[102]
$Ni_{30}Cr_{25}Al_{15}Co_{15}Mo_5Ti_5Y_5$	Al_2O_3	Supersonic particle deposition	Air pressure: 80–90 Pa, C_3H_8 pressure: 60–75 Pa, Ar pressure: 30–40 MPa, H_2 flow rate: 30–40 L/min, powder speed: 5–10 r/min, spray speed: 1000–2000 mm/s, spray distance: 200–250 mm	Friction and wear properties were ensured combined with α-Al_2O_3 strengthening phase	[103]

Table 5 continued

Type	Ceramic particle	Preparation	Process parameter	Performance	References
FeCoNiCrMn	Al_2O_3	Cold spray	Gas pressure: 3 MPa, gas temperature: 300 °C, spraying distance: 30 mm, nozzle traversal speed: 100 mm/s	HEA-based coatings exhibited significantly lower wear rates compared to base material of 6082 aluminum alloy ((12–22) × 10^{-3} mm^3 N^{-1} m^{-1})	[104]
AlCoCrFeNi	WC	High-velocity oxygen fuel spraying	Oxygen flow: 1700 m^3/h, kerosene flow: 0.030 m^3/h, carrier gas flow: 23 m^3/h, spraying distance: 370 mm, rotating speed of powder feeder: 5 r/min, spraying angle: 90°, moving speed of spray gun: 280 mm/s	At flow velocity of 900 r/min, volume loss of AlCoCrFeNi coating was approximately double that of AlCoCrFeNi + 50 wt.% WC–10Co coating	[105]
AlCoCrFeNi	WC–10Co	HVOF spraying	Oxygen flow: 802.2 L/min, spray distance: 380 mm, kerosene flow: 24.6 L/h	Addition of WC–10Co increased microhardness and local plastic deformation resistance of coatings, while it weakened corrosion resistance of coatings	[106]

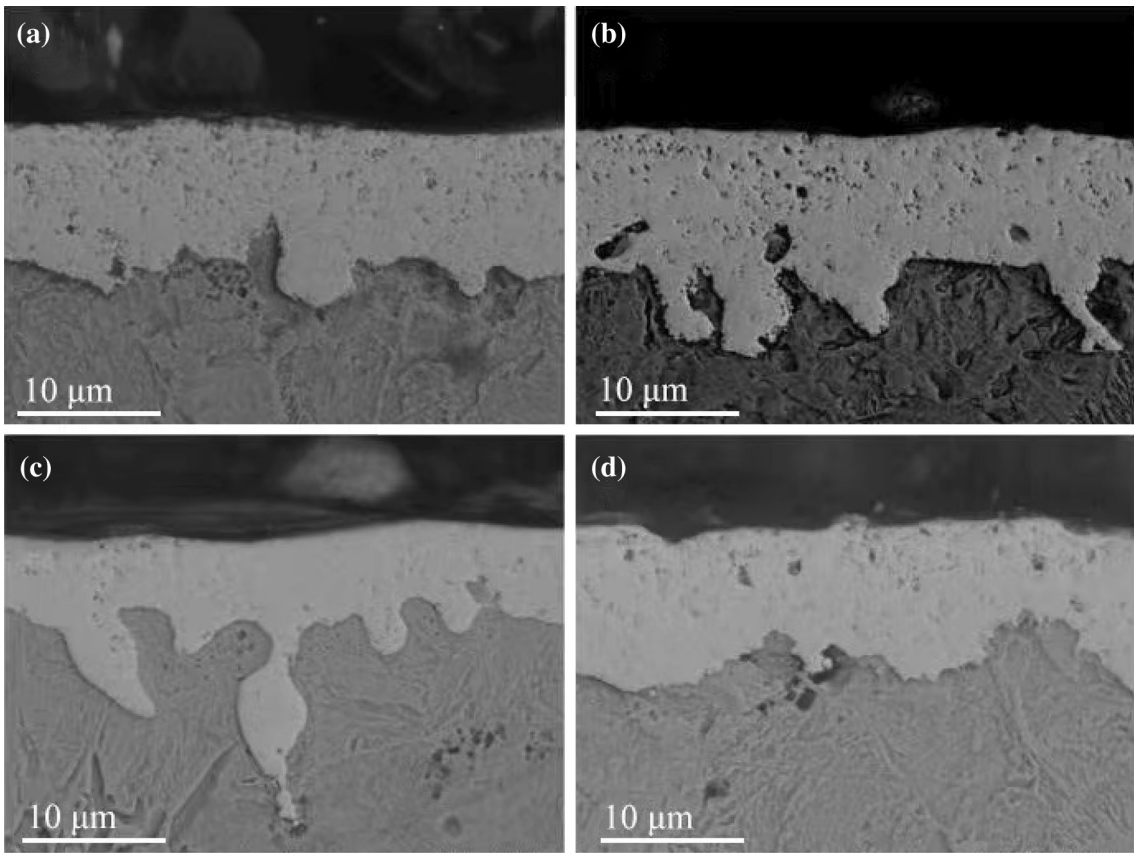

Fig. 3 Scanning electron microscopy (SEM) images of transverse section of niobium carbide coatings deposited using thermo-reactive deposition (TRD) on AISI 1045 steel. **a** 1045-Nb-8 coating; **b** 1045-Nb-12 coating; **c** 1045-Nb-16 coating; **d** 1045-Nb-20 coating [112]

corrosion resistance has also been developed, as indicated in Table 7, which is the preparation process and performance of transition layers that are used for the improvement of adhesion property and service performance of coatings [121–128].

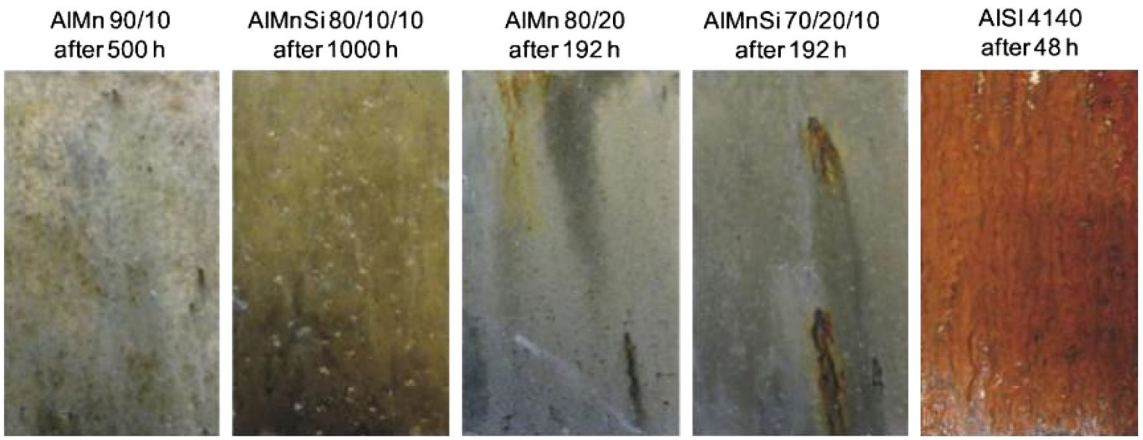

Fig. 4 Images of salt spray test for AISI 4140 steel substrate and substrate–coating systems [114]

Table 6 Preparation processes and performance of diffusion coatings according to latest literature [109–120]

Type	Preparation method	Process parameter	Performance	References
Cr + Al	CVD	Stage 1(Al): 550 °C, 1 h, stage 1(Si): 490 °C, 0.5 h	Higher Al content can achieve a long-term corrosion protection	[109]
VC	DC reactive magnetron sputtering	Total pressure range: 0.3 to 0.6 Pa, power density: 5.5 W cm^{-2}, deposition temperature: 20–500 °C	Impedance increases with C/V ratio, up to 3.27 kΩ cm^2 for C/V = 2.5, in 3.5% NaCl solution	[110]
WC–Co	CVD	920 °C, pressure: 10,526 Pa, Microwave power: 3500 W, H_2 flow: 125 cm^3/min, CH_4 flow: 3 cm^3/min, deposition time: 4 h	With increasing methane concentrations during sputtering, Co diffusion through layer is increased	[111]
NbC	TRD	1020 °C, deposition time: 4 h	Porosity is 0.81998435% within 24 h. Current density measured in 3% NaCl solution is 3.61 × 10^{-5} mA cm^{-2}	[112]
TiN/CrN	PVD	Temperature range: 25–30 °C, time: 20 min, maximum applied voltage: 330 V	R_p (TiN) = 8.9 MΩ cm^2, R_p (CrN) = 161.4 MΩ cm^2	[113]
Al–Mn	Cathodic arc evaporation	400 °C, intensity of pressure: 1 × 10^{-3} Pa, voltage: −10 V, time: 90 min, arc current: 80 A	Current density of AlMnSi (80/10/10) coating and uncoated coating is 0.18 × 10^{-6} and 2.00 × 10^{-6} A cm^{-2}, respectively	[114]
Al	CVD-FBR	550 °C, Ar flow: 1500 mL/min, time: 30–105–180–360 min, HCl in reactive gas mixture: 10.0–6.7–5.0–3.3–2.5 vol.%	An increase in HCl input thicker coatings consisting of Fe–Al intermetallic phase	[115]
Al	CVD	1000 °C, deposition time: 4 h	Diffusion coefficient (β-NiAl) = 1.231013 m^2 s^{-1}, diffusion coefficient (γ′-Ni_3Al) = 4.201014 m^2 s^{-1}, diffusion coefficient (γ-(Ni)) = 3.001014 m^2 s^{-1}	[116]
Ti–6Al–4V	CVD	Temperature: 400–450 °C, total gas pressure: 0.4 Pa, argon gas pressure: 2 Pa, voltage: 1000 V	*Ra* threshold of LV-TPN is higher than limit threshold of 0.1 μm. Fatigue strength after diffusion treatment is higher (11.2 MPa)	[117]
Zn–Mg	PVD	Reaction diffusion time: 20 s, power density: 3 W/cm^2, sputtering time: 10 min, Bias voltage: −200 V, temperature: 350, 380 and 415 °C	I_{corr} of Zn–Mg alloy coating was from 449 to 618 nA cm^{-2}. In contrast, i_{corr} value was 4050 nA cm^{-2} for GI coating. Corrosion rate of Zn–Mg alloy coating is only about 1/9 to 1/6.6 of that of GI coating	[118]
γ-TiAl	PVD	Temperature: $T_{sub} \leq 300$ °C, argon gas pressure: 0.4 Pa, Bias voltage: −50 V, time: 10 min	Effective activation (Q_{kp} = 0.61 EV) and diffusion rate of TGO (1.17 × 10^{-4} ± 1.77 × 10^{-5} A cm^{-2}) are higher than those of oxygen, which can inhibit inward diffusion of oxygen and improve its durability	[119]
TiAlN	PVD	Substrate temperature: 430–460 °C, substrate bias: 40–110 V, deposition pressure: 0.7–4 Pa	Hardness of PVD coating is 1280 HV	[120]

R_p—Polarization resistance; FBR—fluidized bed reactor; LV-TPN—triode plasma nitriding; GI—galvanized iron

4 Organic coatings

Considering environmental and human health issues, the anti-corrosion coatings for low alloy steel are developing toward organic and no-pollution ones. Among these corrosion protection measures, the organic coating is the most widely used, and its cost accounts for two-thirds of all anti-corrosion expenditures. The organic coatings are mainly polymer composite materials with complex/heterogeneous structures and surface/interface diversity in chemical compositions [129, 130]. The polymer resin in the coating can adhere to the metal through chemical bonds or

Table 7 Preparation process and performance of transition layers used for improvement of adhesion property and service performance of metallic coatings [121–128]

Transition layer	Preparation method	Process parameter	Performance	References
Cr/CrN_x	Plasma-enhanced magnetron sputtering	Power: 6 A, frequency: 50 kHz, duty cycle: 80%, gas: 52.6 vol.% N_2 and 47.3 vol.% Ar, pressure: 0.5 Pa, substrate bias: –50 V	Adhesion force of Cr/CrN_x transition layers was improved to 22.5 and 25.7 N, respectively	[121]
V/Cr	Laser cladding	Power: 1500 W, scanning speed: 400 mm/min, beam diameter: 3 mm, overlap rate: 50%	Thickness of V and Cr transition layers reached 700 and 900 μm, respectively	[122]
NiCrAlYNO/NiCrAlY	Vacuum arc evaporation	Arc current: 200 A, Bias voltage: – 100 V, N_2 flow rate: 100 cm^3/min, O_2 flow rate: 30 cm^3/min, 180–200 °C	Ni + CrAlYNO/NiCrAlY duplex structure promotes growth of exclusive alumina scale	[123]
Functionalized graphene oxide (fGO)	Hydrothermal synthesis	0.2 g/L DMF baths, pH: 4, 5 and 6, magnetic stirrer at 200 r/min for 1 h, immersion of steel for 1 h and then cured at 120 °C for 1 h	Improvement of adhesion properties of epoxy coating, R_{ct} = 13,952 Ω cm^2 for fGO treated in ethanol/epoxy, 4 h in 3.5 wt.% NaCl	[124]
MAO	MAO equipment with a bi-directional pulse power	i = 10 A/dm^2, frequency was 200 Hz, positive/negative duty cycle: 30%/10%, 20 min	Shear strength of ACP coating is enhanced by 117% by introducing a MAO(AP) layer	[125]
$FeAl_2$	Magnetron sputtering	Pressure: 2 × 10^{-4} Pa, sputtering power: 300 W, time: 2 h, Ar gas flow rate: 50 cm^3/min, working pressure: 0.5 Pa	$FeAl_2/Al_2O_3$ coating exhibited best adhesive force of 49.75 N	[126]
SiC	Model assumptions	Function $y = A\sin(2\pi x/\lambda)$, which is used for interface shape of SiC transition layer	An interface of sine possessed largest compressive stress and lowest tensile stress	[127]
Ni25	Laser cladding	Laser power: 2000 W, scanning speed: 240 mm/min, Ar: 10 L/min, optical channel diameter: 40 mm, powder feeding speed: 9 g/min	An excellent metallurgical bonding of Ni25/Fe104 composite coating was obtained	[128]

A—Amplitude; λ—wavelength; i—positive/negative current density; DMF—dimethyl formamide; MAO—micro-arc oxidation; ACP—aluminum-chromium phosphate

mechanical action, and then, the physical barrier formed separates the metal surface from the corrosive medium, thereby hindering the penetration of corrosive ions and/or formation of corrosive galvanic cells. According to the existing studies, the organic coatings can be divided into conductive polymer coatings, shielding polymer coatings, and smart coatings.

4.1 Conductive polymer coatings

Conductive polymer coatings refer to the conjugated polymer with π bond in the main chain where the electrons can easily migrate. Electrochemical deposition and electroless plating are the most commonly used methods to prepare conductive polymer coatings. Currently, a significant body of conductive polymers have been developed, among which the conducting polymers of polyheterocyclic compounds with good stability, such as polyaniline (PANI) [131–134], polypyrrole (PPY) [135–137], polythiophene (PTH) [138, 139], poly-p-phenylene (PPPH) [140] and poly-p-phenylene vinylene (PPV) [141], are the most widely used conductive polymers. Conductive polymers, which combine the characteristics of metals/polymers and have excellent physical and chemical properties, have achieved extensive interests in the field of anti-corrosion coatings [142–144]. The comparison regarding preparation and performance of these conducting polymers according to the latest literature [131–154] is followed as Table 8.

According to the existing literature, the anti-corrosion mechanism of the conductive polymer coatings can be divided into the following aspects:

1. The conductive polymer coatings have a dense structure and remains excellent adhesion to the metal substrate, acting as a physical barrier to effectively inhibit the direct contact of water, oxygen, corrosive ions, etc., with the protected metal substrate [144].
2. The oxidation of the metal substrate can be promoted by its own oxidation–reduction reaction which can form a dense oxide layer at the interface, and the occurrence of subsequent corrosion is further suppressed [145–149].

Table 8 Preparation processes and performance of conductive polymer coatings according to latest literatures [131–154]

Type	Process parameter	Performance	References
PANI/epoxy	2 g PANI into 100 mL of 2 mol/L H_3PO_4, 44 mol/100 g epoxy resin into 6% acid-doped PANI. Process: (25 °C, 30% RH) for 12 h, then 40 °C for 12 h, and finally 25 °C for 168 h	$\|Z\|_{0.01\ Hz} = 2.3 \times 10^9\ \Omega\ cm^2$ after 100 days of immersion of PANI-SSA/epoxy in 3.5% NaCl at room temperature	[131]
PANI@MoS_2	MoS_2 into 50 mL of 1 mol L^{-1} HCl, ultrasonically dispersing for 30 min, adding 2 mL of aniline, stirring for 1 h, then adding 50 mL of 1 mol L^{-1} HCl with 1.254 g APS into above solution, stirred at 0–5 °C for 12 h and vacuum drying at 60 °C for 24 h	$\|Z\|_{0.01\ Hz} = 10^{4.93}\ \Omega\ cm^2$, $I_{corr} = 1.69 \times 10^{-7}$ A cm^{-2} of 8%i-PANI@MoS_2-7/EP after 24 h in 3.5% NaCl at room temperature	[132]
PANI@ZnP	1.8 g CTAB into 10 mL toluene under sonication for 30 min, adding this solution into 0.93 g Ani, 0.5 g H_3PO_4 and 50 mL deionized water under sonication for 10 min, 2.28 g APS in 10 mL deionized water, final mixture for 5 min, freezing for 24 h and drying in a vacuum for 12 h at 50 °C	$\|Z\|_{0.01\ Hz} = 2.5 \times 10^5\ \Omega\ cm^2$ of ER/PANI@ZnP after 168 h in 3.5 wt.% NaCl at room temperature	[133]
PANI/epoxy	4 g potassium hexacyanoferrate into 28 g H_3PO_4, stirring at 25 °C for 1.5 h, mixing 25 g epoxy resin E-44, 3 g xylene, and 10 g absolute ethanol at 50 °C, adding 4.23 g H_3PO_4 into solution A	$\|Z\|_{0.01\ Hz} = 5.27 \times 10^6\ \Omega\ cm^2$, $I_{corr} = 1.01 \times 10^{-8}$ A cm^{-2} of PUM15 after 24 h in 3.5 wt.% NaCl at room temperature	[134]
Ti–PPY	A: 0.05 mol/L pyrrol (Py) into 30 μL toluene, B: phytic acid into 3.5 mL phosphate buffer, and mixing A, B and ethanol. Electro-polymerization: a galvanostatic current procedure at 0.5 mA cm^{-2} for 180 s and 0.9 mA cm^{-2} for 100 s	$\|Z\|_{0.01\ Hz} = 2 \times 10^4\ \Omega\ cm^2$ in 0.05 mol/L PA with PPY at room temperature	[136]
PPY-functionalized BN sheets	10 g epoxy resin into ethanol suspension containing BNNS, f-BNNS, and/or PPY, vigorous stirring for 2 h	$\|Z\|_{0.01\ Hz} = 1.9 \times 10^7\ \Omega\ cm^2$ after 40 days of f-$BNNS_{0.5}$-PPy_3/EP in 3.5 wt.% NaCl at room temperature	[137]
PT-ETMS/MnO_2	PT and MnO_2 nanoparticles were mixed in a solvent (xylene:n-butanol = 7:3, 40 wt.%), and then thermally cured at 150 °C for 1 h	$R_c = 1.32 \times 10^4\ \Omega\ cm^2$ after 80 days. $I_{corr} = 297.75$ nA cm^{-2} in seawater at room temperature	[139]
PANI-PA	0.4 mol/L distilled aniline into 250 mL of 0.5 mol/L phytic acid solution, and then 250 mL of 0.5 mol/L ammonium peroxydisulfate solution into phytic acid solution with constant stirring for 6.5 h in an ice bath, temperature at 0–5 °C	$R_{ct} = 4.4 \times 10^8\ \Omega\ cm^2$ after 50 days in 3.5 wt.% NaCl at room temperature	[148]
V-TiO_2/PPY CTs	Solutions contained 0.3 mol/L oxalic acid, 0.1 mol/L pyrrole and 1 g L^{-1} TiO_2 NPs or V-TiO_2 NPs. Purging with N_2 gas for 15 min. Cyclic scans were carried out with potential range from −0.5 to 0.9 V for 30 scanning circles and scanning rate was 50 mV s^{-1}	$I_{corr} = 41.5 \pm 5.8$ mA cm^{-2} of V-TiO_2/PPY in 0.1 mol/L HCl at room temperature	[153]
SiO_2@PANI	20 mg SiO_2@PANI and 1 g silicone were dispersed in 1.5 mL THF under ultrasonic agitation for 2 h	$\|Z\|_{0.01\ Hz} = 2.24 \times 10^7\ \Omega\ cm^2$ for 4:1 in 0.1 mol/L H_2SO_4 at room temperature	[154]

$|Z|_{0.01\ Hz}$—Impedance modulus at a frequency of 0.01 Hz; R_c—coating resistance; SSA—sulfonylsalicylic acid; CTAB—cetyl-trimethyl ammonium bromide; Ani—Aniline; BNNS—hexagonal boron nitride nanosheet; f-BNNS—functionalized BNNS; PT-ETMS—phlythiophene ethyltrimethoxysilane; PT—phlythiophene

3. The reduction of the conductive polymer and/or the ion exchange between the coatings and the corrosive environment will be accompanied by the de-doping process of the dopant anion during the service stage. Some special doping ions, e.g., phosphomolybdate, sulfonate, etc., can be complexed with the metal cation on the metal surface after being de-doped, thereby inhibiting the further corrosion of the metal [150, 151].

Unfortunately, the defects of micro-pores in single conductive polymer coatings have weakened their protective effect on the metal substrate since the corrosive ions can enter the coating/metal interface through these micro-pores in the coating to some degree. In recent years, some conductive polymer composite coatings with few defects and excellent corrosion resistance were explored by compounding conductive polymer coatings with novel materials, like carbon nanotubes and graphene because of their

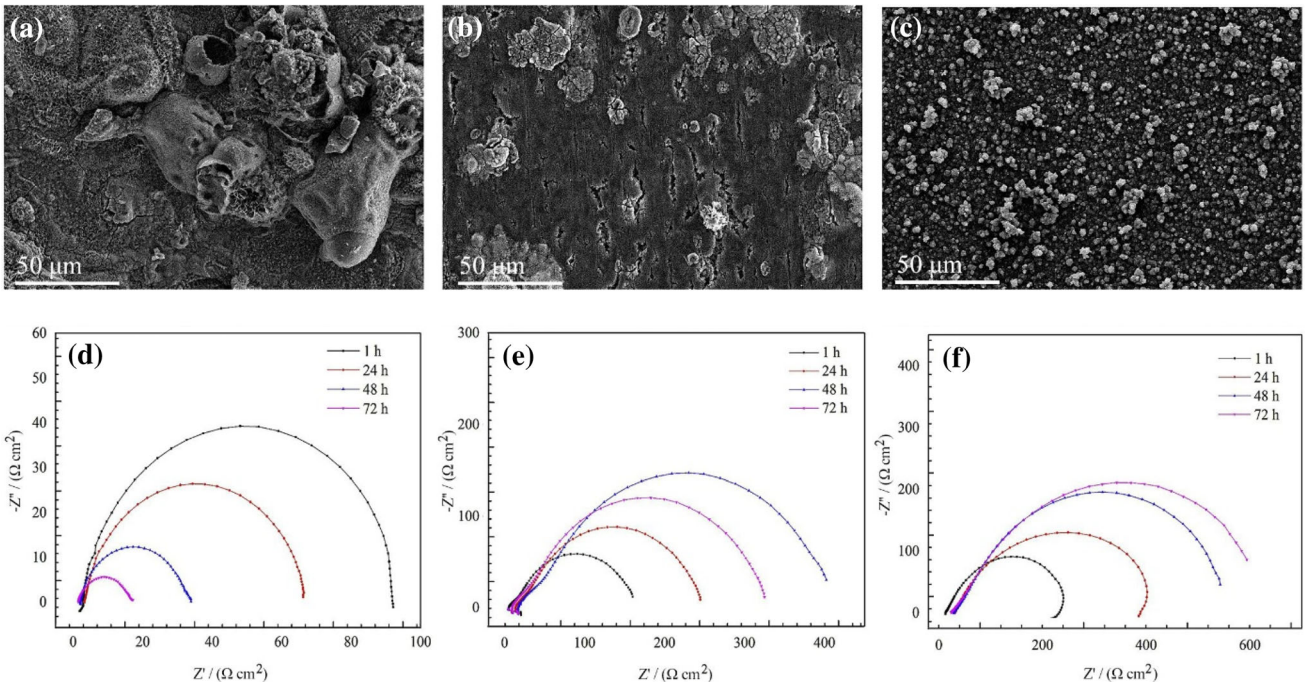

Fig. 5 SEM micrographs (**a**–**c**) and Nyquist plots (**d**–**f**) of bare carbon steel (CS) (**a**, **d**), TiO_2/PPY CC (**b**, **e**) and V-TiO_2/PPY CC (**c**, **f**) after 12 h of immersion in 0.1 mol/L HCl solution [153]. Z'—Real parts of impedance; Z''—imaginary parts of impedance

excellent electrochemical properties and corrosion resistance [152, 153], which has been one of the most attractive topics in the field of organic coatings.

For instance, Shi et al. [154] prepared a PANI-SiO_2 composite coating with hydrophobic properties by combining PANI with modified silica nanoparticles, and the results indicated that the corrosion resistance of the coating was still as high as 99.99% after 71 days of immersion in a 0.1 mol/L H_2SO_4 environment, which can be explained by the modified SiO_2 effectively filling the pores of PANI polymer to form a dense coating structure. Similarly, Deyab [152] compounded carbon nanotube material (CNT) with polyaniline anti-corrosion coatings and found that the porosity/defects of the PANI coating significantly decreased with the increase in the CNT content. The introduction of CNT can enhance a "barrier effect" of the coating, thereby restricting the permeability of corrosive ion, O_2 and water, and improve the corrosion resistance of the coatings. However, the efficient conductivity may be continuously enhanced with the incorporation of CNT owing to the possible presence of electron transfer paths. In a recent study, Chen et al. [153] introduced transition metal vanadium (V) into titanium dioxide (TiO_2) to make nanoparticles and then combined PPY to prepare a V-TiO_2/PPY composite coating with a microscopic size. The combination of PPY and V-TiO_2 effectively prevented the infiltration of corrosive ions in most chloride environments, while the increase in conductivity of the coating owing to the introduction of V-TiO_2 would accelerate the formation of oxide films on the metal surface. And under the synergistic effect of the two, the charge transfer in the corrosion system was inhibited, and the passivation state of the metal surface was thus maintained (Fig. 5).

In addition, the graphene sheet as a filler can effectively hinder the diffusion of gas and liquid molecules because of its high impermeability and specific surface area. The inorganic characteristic of graphene can significantly enhance the compatibility of the coating with the substrate and improve the shielding performance of the conductive polymer coatings against corrosive media. However, the high conductivity of graphene makes it easy to induce internal defects in the coatings during electrochemical deposition processes, and cannot obtain the long-term corrosion resistance. Presently, the application of graphene in organic coatings is usually achieved by the combination of graphene-conductive and polymer-shielding polymer, and a series of related literature will be systematically reviewed below.

4.2 Shielding polymer coatings

Shielding polymer coatings are widely used for corrosion protection of steel materials due to their excellent barrier properties, by which the contact between the substrate and corrosive medium is effectively blocked. In the meanwhile, the shielding polymer coating can prevent the charge

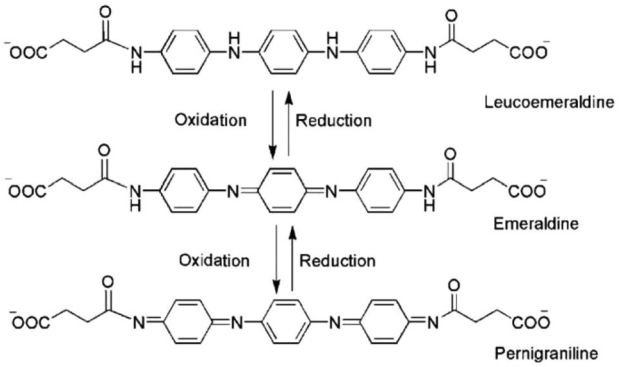

Fig. 6 Molecular structure of CAT in various oxidation states [156]

transfer process between the corrosive medium and metal matrix because of its non-conductivity in long-term corrosive environments, thereby inhibiting the dissolution of metal. Currently, the most common barrier polymer coatings include epoxy resin, inorganic–organic hybrid and so on. However, it is difficult for the traditional shielding polymer coatings to meet the anti-corrosion requirements of modern technologies with the increasingly harsh application environment. Thus, most of literature has focused on the modification of conductive polymers (e.g., carbon nanotubes [155], graphene [156–158], and organic doping [150], etc.) and then combined with the shielding polymer coating to prepare an organic coating that can provide the long-term corrosion resistance and stability.

For instance, a water-soluble carboxylated aniline trimer (CAT) was synthesized by Gu et al. [156], as shown in Fig. 6, through which a stable dispersion of graphene in an aqueous solution was well achieved under the π-π interaction between CAT and graphene, followed by combining with epoxy materials to obtain an epoxy composite coating with excellent corrosion resistance. A similar but more general approach was reported by Qiu et al. [157], who found that the high-concentration dispersed graphene in water can be successfully obtained by using a hydrophilic conductive polymer-PPY nano-colloid as an intercalating agent and ultrasonic technology. The dispersed graphene slurry was mixed with the shielding polymer E-51 epoxy resin to prepare the graphene-PPY-epoxy resin composite coating, in which 2θ can be defined by XRD scanning angle (Fig. 7). The results showed that the density and corrosion resistance of the coating significantly increased with the addition of the conductive polymer-PPY. Additionally, Ramezanzadeh et al. [158] combined graphene and conductive polymer-PANI composite nanoparticles with zinc-rich epoxy resin to prepare a composite coating with cathodic protection characteristic. A galvanic couple was formed between zinc and the steel substrate since the zinc as the anode could inhibit the corrosion of the steel substrate as the cathode. On the other hand, the addition of graphene can reduce the pore defects of the coating and enhance the shielding effect of the layer on corrosive ions.

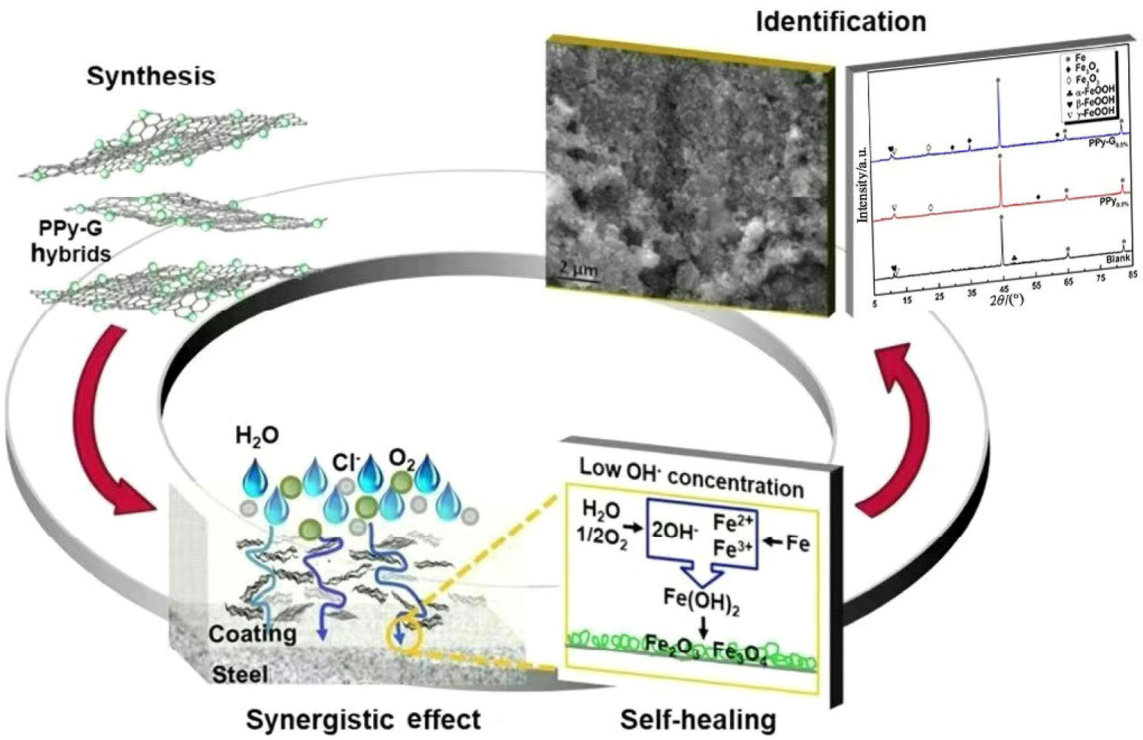

Fig. 7 Synergistic mechanism of polypyrrole-intercalated graphene for enhanced corrosion protection [157]

In the meanwhile, the PANI can promote the electrical contact between zinc and the substrate and reduce the oxidation of zinc, thereby achieving the long-term and stable corrosion resistance of the coating.

In comparison, Pour-Ali et al. [150] doped a macromolecular organic substance-camphor sulfonic acid (CSA) into the conductive polymer coating (PANI) and then combined it with a typical shielding polymer coating (epoxy resin). And the technique assembled with epoxy resin can significantly reduce the defects of PANI itself, improve the physical barrier effect of the coating, and effectively prevent the inward diffusion of corrosive ions. Moreover, PANI formed a passivation layer at the coating/steel interface and then CSA reacted with Fe^{2+} released from the surface of the substrate to form insoluble composites to fill the passivation layer and coating defects. Despite these advantages, some obstacles, including large-scale production, wear resistance and high-temperature environment, have limited the further industrial use of these coatings.

4.3 Smart self-healing coating

Currently, most protective coatings are still largely based on passivation; however, some damages caused by environmental and mechanical attacks may be inevitable, and if the film damage cannot be repaired in a timely and effective manner, corrosive ions will penetrate the coating, followed by the failure of the coating. Thus, it is a pioneering research topic to develop a new generation of smart (and environmentally friendly) coatings, where active components will be incorporated into a passive/barrier matrix to achieve a self-healing coating system owning instant feedback to changes in the local environment for future high-tech applications of low alloy steel. A timeline illustrating the development of smart self-healing coatings is provided in Fig. 8. The pioneering research work in the field of self-healing anti-corrosion coatings is from the group of Kumar et al. [159–162]. The main idea is concentrated on pre-storing the corrosion inhibitor in moderation, and the corrosion inhibitor can migrate to the damaged position in time and actively repair the damage in the coating, followed by the formation of a new barrier, thereby achieving a self-healing of coatings. Ideally, such active self-healing coating system provides low alloy steel a super prolonged and robust protection against corrosion. The global scholars have carried out a lot of research work on the development and repair mechanism of smart coating systems, which has become a frontier and hot topic in the field of metal material corrosion and protection.

There are generally two methods of designing the self-healing coatings, e.g., an addition of direct dispersion and nano-containers for loading active agents. The direct dispersion refers to the addition of active agents like corrosion inhibitors into the coating. When the coating is damaged, the corrosion inhibitor can quickly penetrate into the coating defect and inhibit the electrochemical reaction of the exposed metal substrate [163]. However, the self-healing process is restricted by the number of repairs, and once the active agent is completely released, it will leave a diffusion channel for the corrosive media owing to the damage of the integrity of the coating, followed by the occurrence of metal corrosion. In addition, the reagents directly dispersed in the coating may interact with the coating substrate and affect its adhesion and sealing performance. In comparison, the encapsulation addition of

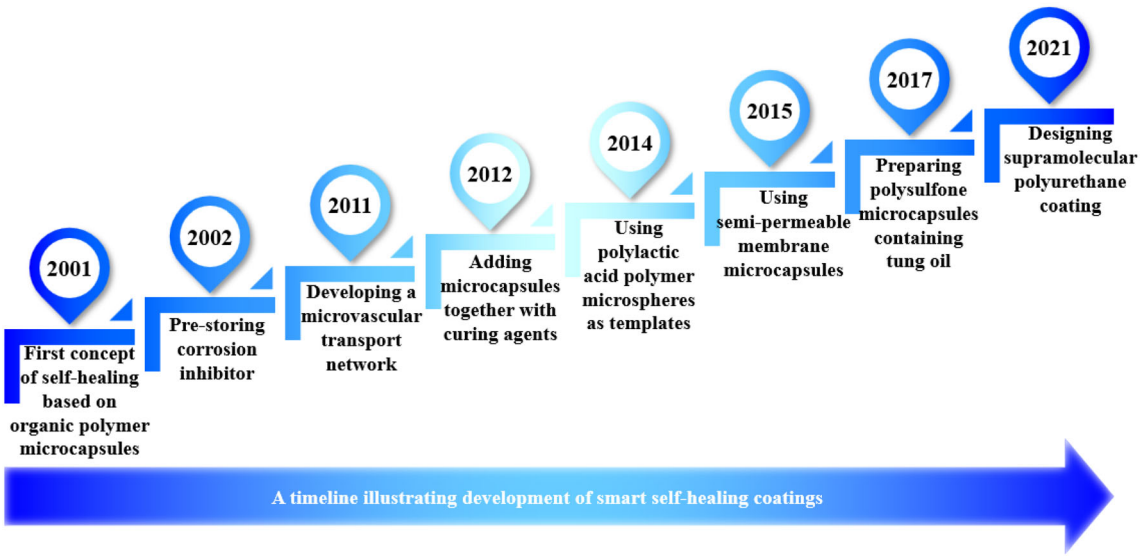

Fig. 8 A timeline illustrating development of smart self-healing coatings

active agents into nano-containers can effectively weaken the adverse effects of direct dispersion on the coating, while it also achieves the self-healing function of the coating.

White et al. [164] first proposed the concept of self-healing based on organic polymer microcapsules in 2001, in which the polyurea-formaldehyde microcapsules encapsulated with self-healing components were prepared through traditional in situ emulsion polymerization to achieve the self-healing of the damaged area and maintain the integrity of the original coating structure (Fig. 9). The emergence of the microcapsule-based self-healing system has promoted the development of the self-healing field and received extensive attention, and the principle is shown in Fig. 9.

In addition, other types of microcapsule-based self-healing materials have been developed and applied in the past 20 years [165–168]. For instance, the polyurea-formaldehyde resin microcapsules filled with a large amount of epoxy resin have been successfully prepared by in situ polymerization, in which the microcapsules containing self-healing components together with corresponding curing agents have been added into the traditional epoxy matrix [169]. The mechanism lies in the contact of active components with curing agents under the effect of external force to fill the cracks and restore the original anti-corrosion function. Li et al. [170] prepared polysulfone microcapsules containing tung oil by solvent evaporation, with an average particle size of about 130 μm and a wall thickness of about 9 μm, and then added them into epoxy matrix. The corrosion results showed that the scratched coating still exhibited excellent corrosion resistance after being immersed in chloride solutions for 7 days.

Although the microcapsule-based polymer self-healing coating has some advantages, it is still faced with some shortcomings, e.g., the one-time characteristic, and the failure of microcapsules will be inevitable when the microcapsules release the healing agent and realize the self-repair of the coating. In order to overcome this problem, the semi-permeable membrane microcapsules can be used to regulate and control the release of encapsulated self-healing agents [171]. Unfortunately, the self-healing process may be affected by the crack direction since the occurrence of cracks is common issue after the coating being destroyed. Thus, the self-healing efficiency based on microcapsule-type coatings will inevitably be lower than the theoretical value. The key ideas behind this issue should be touched. Firstly, a large amount of self-healing agents are necessary to achieve the multiple self-repair functions of the coating at the same damage site. On the other hand, the self-healing agents should continuously flow into the damaged location. In this regard, researchers developed a microvascular transport network and

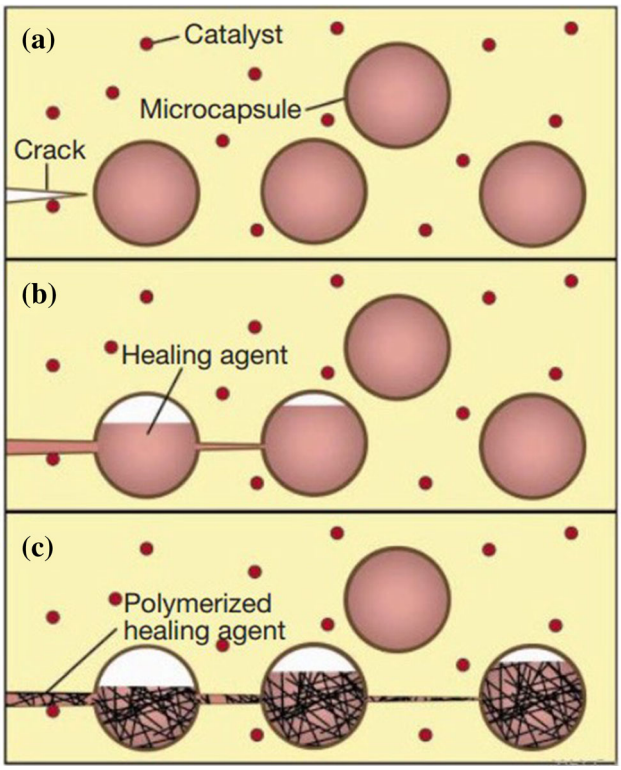

Fig. 9 Autonomic healing concept showing that a microencapsulated healing agent is embedded in a structural composite matrix containing a catalyst capable of polymerizing healing agent. **a** Cracks form in matrix wherever damage occurs; **b** microcapsules ruptured by crack, releasing healing agent into crack plane through capillary action; **c** healing agent contacting catalyst and triggering polymerization that bonds crack faces closed [164]

embedded the device in a self-healing polymer coating [172–174]. However, these technologies can only be applied for preparation of smaller-size coatings, and it is difficult to prepare microvascular network self-healing materials on a large scale. In recent years, researchers created a new microvascular network by using polylactic acid polymer microspheres or fibers as templates, ensuring the coatings with multiple and efficient self-healing capabilities, as shown in Fig. 10 [175–177].

Krull et al. [177–179] developed a method to realize the self-healing function of large-scale coating damage, in which the coating was composed of epoxy polymer and micro-channels. In the case of millimeter-level damage, the self-healing agents in the micro-vessel can be transported to the damage site under the control of external pressure and achieve the self-healing of coatings; the central puncture and lost volume are restored with two-stage healing agents via a dual microvascular network. The radiating microcracks are healed by reactive solutions released from ruptured microcapsules (Figs. 11 and 12). Moreover, in recent research by Gergely et al. [177], the self-healing of damage in the millimeter scale can be well

achieved after using microcapsules and microvascular strategies to modify polymer coatings, which will provide the possibility for the large-scale preparation of self-healing coatings with microvascular networks. In recent years, a broad spectrum of works regarding smart self-healing coatings are available, which further provides a critical overview on the fundamental understanding, novel preparation techniques and mechanism in the latest three years [180–191]. Although the self-healing coating of the microvascular network system has many advantages, it is still necessary to consider the cost of the microvascular network self-healing material in the production process and controllable issues in the transportation of self-healing agents in the microvasculature, and it can ensure the circulation of the self-healing agents in the micro-vessels of coatings and the feasibility of multiple self-healing processes. In general, the organic coating is more environmental technique compared to many conventional coatings, and in the future, more pressure will be put on this sector too.

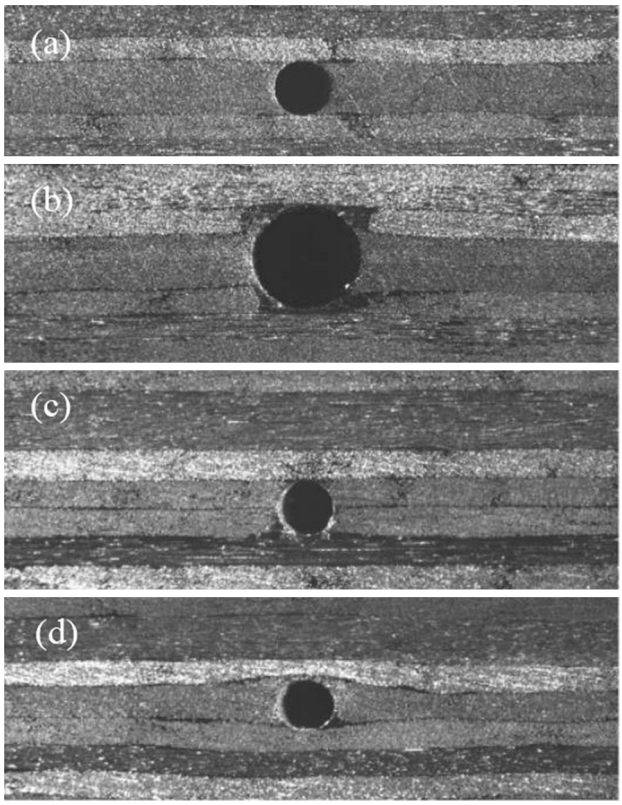

Fig. 10 Vascular morphologies. **a** 0.25B_C; **b** 0.5B_C; **c** 0.25B_A; **d** 0.25A_A [176]

5 Conclusions

As mentioned earlier, it is inevitable for low alloy steel to contact with the corrosive media from atmosphere, water, soil as well as other external environments during the long-term service condition. Based on the requirement of corrosion resistance, selecting the corresponding coating is of central importance to extend the service life of low alloy steel and maintain production and life safety. This article exclusively consolidates the information related to the preparation, advantages and disadvantages, applications and research progress of various types of protective coatings suitable for low alloy steel surfaces based on the latest published literature. Based on this, the prospects for the

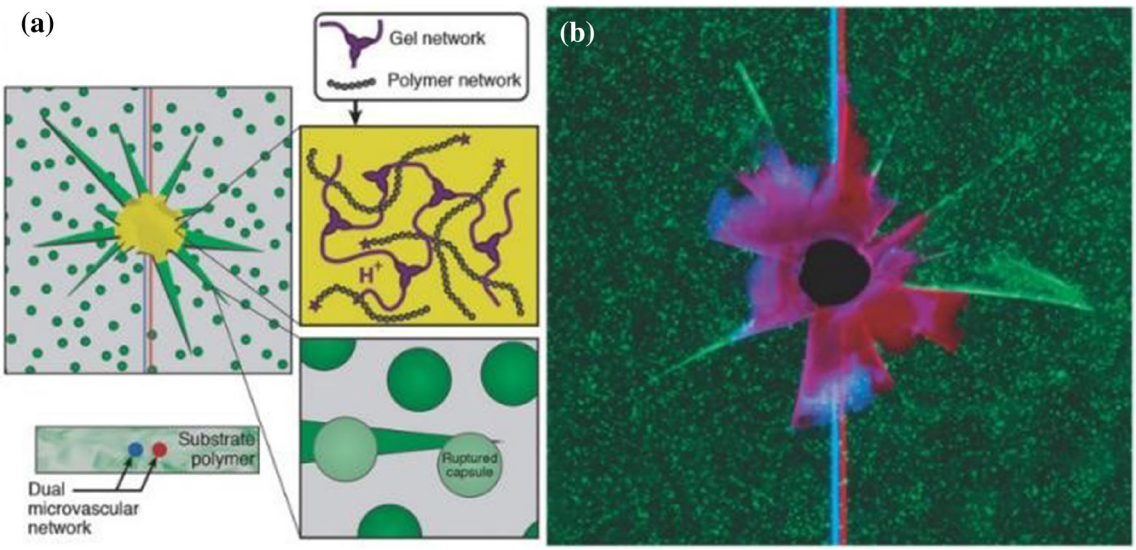

Fig. 11 Hybrid microcapsule–microvascular self-healing system. **a** Schematic of hybrid self-healing system; **b** optical image of hybrid specimen during filling of damage with two-stage healing agents [177]

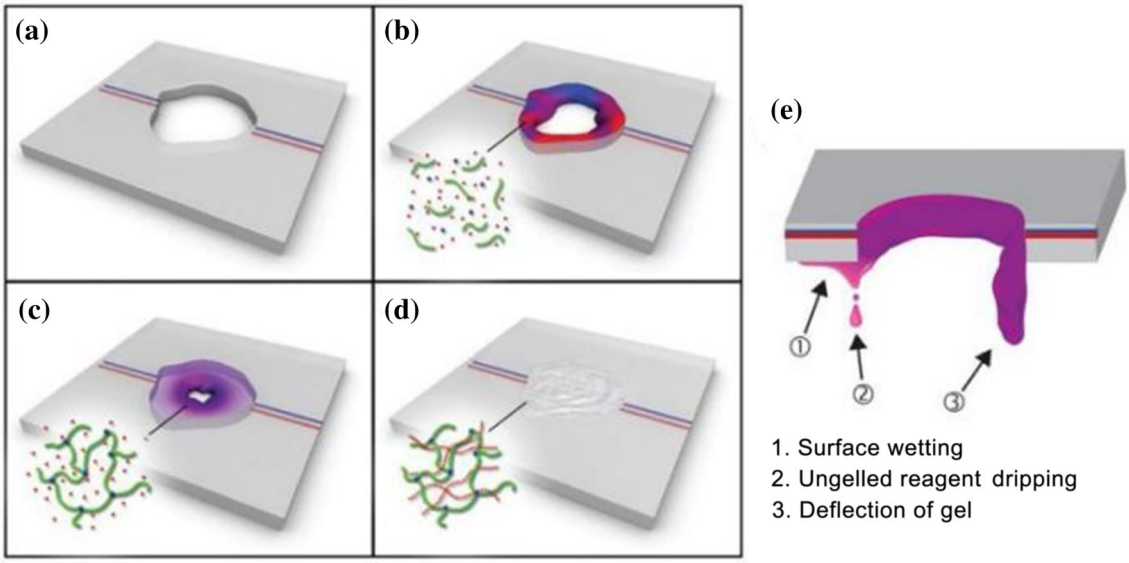

Fig. 12 Schematic showing regenerative process for a two-stage healing agent system [178]

development of anti-corrosion coatings on the surface of low alloy steel are summarized as follows.

With a gradual increase in global environmental protection awareness, the environmentally unfriendly traditional coatings and corresponding coating technologies are subjected to restrictions in the application range, whereas the environmentally friendly multifunctional organic coatings have received extensive attention owing to their excellent corrosion resistance and self-healing characteristics. In addition, the coating techniques are becoming more and more simplified and green; however, their applications are often restricted by increased production cost and industrialization difficulty. On the whole, the modification of traditional metal coatings and the development of new organic smart coatings under the consideration of environmental protection, low cost, simplicity and large-scale industrial application are simultaneously proceeding. Thus, no matter from the perspective of scientific research or industrialization, the protective coatings on low alloy steel are still of great potential and one of the most active areas of material science.

Acknowledgements This paper is supported by Key Scientific Research Project in Shanxi Province (Grant Nos. 201903D111008 and 202003D111001), National Natural Science Foundation of China (Grant No. 52071227), Fundamental Research Program of Shanxi Province (Grant No. 202103021223293), Scientific and Technological Innovation Programs of Higher Education Institutions in Shanxi (Grant No. 2021L306), Scientific Research Fund of Taiyuan University of Science and Technology (Grant No. 20202044), Award Fund for Outstanding Doctors in Shanxi Province (Grant No. 20212041), and Postgraduate Education Innovation Project of Shanxi Province (Grant Nos. 2022Y686 and 2022Y684).

Declarations

Conflict of interest The authors declare that there are no conflicts of interest and ethical rule that could have appeared to influence the work reported in this paper.

References

[1] Z. Liu, X. Gao, J. Li, L. Du, C. Yu, P. Li, X. Bai, Electrochim. Acta 213 (2016) 842–855.
[2] W.J. Peng, G.X. Wu, Y. Cheng, J.Y. Zhang, J. Iron Steel Res. Int. 26 (2019) 1304–1314.
[3] X.W. Feng, J. Xie, W.Y. Xue, Y.F. Shen, H.B. Wang, Z.Y. Liu, J. Iron Steel Res. Int. 26 (2019) 472–482.
[4] J.S. Wang, P.Y. Shi, C.J. Liu, M.F. Jiang, J. Iron Steel Res. Int. 22 (2015) 1020–1023.
[5] S. Zhang, Y. Li, Y. Wei, B. Liu, H. Du, H. Wei, L. Hou, Vacuum 185 (2021) 110042.
[6] S. Zhang, Y. Li, B. Liu, L. Mou, S. Yu, Y. Zhang, X. Yan, Vacuum 196 (2022) 110790.
[7] S. Zhang, Y. Li, Y. Wei, B. Liu, L. Hou, H. Du, X. Liu, Chin. J. Mater. Res. 35 (2021) 721–731.
[8] R.M. Geng, J. Li, C.B. Shi, J. Iron Steel Res. Int. (2022) https://doi.org/10.1007/s42243-022-00751-1.
[9] S.R. Wang, J.W. Yang, J.P. Cao, S. Jiang, F.F. Xu, J. Iron Steel Res. Int. 29 (2022) 698–706.
[10] S. Singh, K. Goyal, R. Bhatia, Mater. Today Proceed. 56 (2022) 379–383.
[11] S. Pourhashem, A. Seif, F. Saba, E.G. Nezhad, X. Ji, Z. Zhou, X. Zhai, M. Mirzaee, J. Duan, A. Rashidi, B. Hou, J. Mater. Sci. Technol. 118 (2022) 73–113.
[12] F. Wang, J. Liu, L. Liang, Y. Luo, T. Xiong, M.S. Balogun, Z. Wang, R. Yu, Int. J. Hydrogen Energy 47 (2022) 9946–9957.
[13] L. Zhao, D. Ouyang, Y. Wang, K. Chan, J. Non-Cryst. Solids 586 (2022) 121559.
[14] C. Zhong, F. Liu, Y. Wu, J. Le, L. Liu, M. He, J. Zhu, W. Hu, J. Alloy. Compd. 520 (2012) 11–21.

[15] G. Dai, S. Wu, X. Huang, J. Alloy. Compd. 902 (2022) 163736.
[16] M.H. Nazari, Y. Zhang, A. Mahmoodi, G. Xu, J. Yu, J. Wu, X. Shi, Prog. Org. Coat. 162 (2022) 106573.
[17] M.M. Sreejaya, R.J. Sankar, R.K.N.P. Pillai, K. Ramkumar, P. Anuvinda, V.S. Meenakshi, S. Sadanandan, Mater. Today Proceed. 60 (2022) 494–501.
[18] I.I. Udoh, H. Shi, E.F. Daniel, J. Li, S. Gu, F. Liu, E.H. Han, J. Mater. Sci. Technol. 116 (2022) 224–237.
[19] G. Cui, Z. Bi, S. Wang, J. Liu, X. Xing, Z. Li, B. Wang, Prog. Org. Coat. 148 (2020) 105821.
[20] S. Oukach, B. Pateyron, L. Pawłowski, Surf. Sci. Rep. 74 (2019) 213–241.
[21] O.S.I. Fayomi, I.G. Akande, O.P. Abioye, O.B. Fakehinde, Proced. Manufact. 35 (2019) 1007–1012.
[22] J. Tang, Y. Zuo, Corros. Sci. 50 (2008) 2873–2878.
[23] M. Bello, S. Shanmugan, J. Alloy. Compd. 839 (2020) 155510.
[24] Y. Kuzminykh, A. Dabirian, M. Reinke, P. Hoffmann, Surf. Coat. Technol. 230 (2013) 13–21.
[25] L. Zhu, P. Xue, Q. Lan, G. Meng, Y. Ren, Z. Yang, P. Xu, Z. Liu, Opt. Laser Technol. 138 (2021) 106915.
[26] B. Shi, S. Huang, P. Zhu, C. Xu, P. Guo, Y. Fu, Mater. Lett. 276 (2020) 128093.
[27] V.V.S. Yedida, H. Vasudev, Mater. Today Proceed. 50 (2022) 1458–1464.
[28] Z.F. Yuan, S.S. Xie, X.T. Yu, J. Liu, P. Du, Z.H. Li, J. Iron Steel Res. Int. 26 (2019) 123–129.
[29] P. Kwakhong, A. Artnaseaw, C. Kruehong, J. Iron Steel Res. Int. 22 (2015) 746–751.
[30] Š. Houdková, F. Zahálka, M. Kašparová, L.M. Berger, Tribol. Lett. 43 (2011) 139–154.
[31] M.S. Safavi, F.C. Walsh, Surf. Coat. Technol. 422 (2021) 127564.
[32] D.P. Weston, P.H. Shipway, S.J. Harris, M.K. Cheng, Wear 267 (2009) 934–943.
[33] Q. Wang, L.L. Zhai, L. Zhang, J.W. Zhang, C.Y. Ban, J. Mater. Res. Technol. 17 (2022) 2145–2157.
[34] G. Qiao, T. Jing, N. Wang, Y. Gao, X. Zhao, J. Zhou, W. Wang, Electrochim. Acta 51 (2005) 85–92.
[35] A. Karimzadeh, M. Aliofkhazraei, F.C. Walsh, Surf. Coat. Technol. 372 (2019) 463–498.
[36] C. Sun, J. Li, S. Shuang, H. Zeng, J.L. Luo, Corros. Sci. 134 (2018) 23–37.
[37] H. Luo, M. Leitch, H. Zeng, J.L. Luo, Mater. Today Phys. 4 (2018) 36–42.
[38] C. Sun, H. Zeng, J.L. Luo, Corros. Sci. 148 (2019) 317–330.
[39] C. Sun, J. Li, V. Fattahpour, M. Roostaei, M. Mahmoudi, H. Zeng, J.L. Luo, Corros. Sci. 166 (2020) 108422.
[40] J. Wojewoda-Budka, A. Wierzbicka-Miernik, M. Szczerba, H. Kazimiercza, I. Kwiecien, J. Morgiel, K. Stan-Glowinska, F. Valenza, Mater. Charact. 171 (2021) 110811.
[41] P. Bera, H. Seenivasan, K.S. Rajam, V.K.W. Grips, Appl. Surf. Sci. 258 (2012) 9544–9553.
[42] V.E. Selvi, H. Seenivasan, K.S. Rajam, Surf. Coat. Technol. 206 (2012) 2199–2206.
[43] X. Zhang, F. Wang, Y. Zhou, A. Liang, J. Zhang, Surf. Coat. Technol. 352 (2018) 42–48.
[44] M. Barzegar, S.R. Allahkaram, R. Naderi, N. Ghavidel, Wear 422–423 (2019) 35–43.
[45] M. Fathi, M.S. Safavi, S. Mahdavi, S. Mirzazadeh, V. Charkhesht, A. Mardanifar, M. Mehdipour, Tribol. Int. 159 (2021) 106956.
[46] B. Huang, C. Zhang, G. Zhang, H. Liao, Surf. Coat. Technol. 377 (2019) 124896.
[47] G.Y. Koga, R. Schulz, S. Savoie, A.R.C. Nascimento, Y. Drolet, C. Bolfarini, C.S. Kiminami, W.J. Botta, Surf. Coat. Technol. 309 (2017) 938–944.
[48] G. Ji, O. Elkedim, T. Grosdidier, Surf. Coat. Technol. 190 (2005) 406–416.
[49] Y. Guo, G.Y. Koga, A.M. Jorge Jr., S. Savoie, R. Schulz, C.S. Kiminami, C. Bolfarini, W.J. Botta, Mater. Des. 111 (2016) 608–615.
[50] G. Liu, Y. An, Z. Guo, J. Chen, G. Hou, J. Chen, Appl. Surf. Sci. 258 (2012) 5380–5386.
[51] Y.Y. Zhou, G.Z. Ma, H.D. Wang, G.L. Li, S.Y. Chen, H.J. Wang, M. Liu, Mater. Des. 110 (2016) 332–339.
[52] J.C. Lin, C.L. Liu, J.J. Lee, T.P. Liu, W.C. Ko, Y.C. Huang, C.H. Wu, Y.J. Chen, Int. Immunopharmacology 15 (2013) 333–339.
[53] X. Zhang, Z. Wang, J. Lin, Z. Zhou, Surf. Coat. Technol. 283 (2015) 255–261.
[54] Q. Luo, Y.J. Sun, J. Jiao, Y.X. Wu, S.J. Qu, J. Shen, Surf. Coat. Technol. 334 (2018) 253–260.
[55] Y. An, G. Hou, J. Chen, X. Zhao, G. Liu, H. Zhou, J. Chen, Vacuum 107 (2014) 132–140.
[56] Y. Wang, Z. Xing, Q. Luo, A. Rahman, J. Jiao, S.J. Qu, Y.G. Zheng, J. Shen, Corros. Sci. 98 (2015) 339–353.
[57] J.H. Qiao, X. Jin, J.H. Qin, H.T. Liu, Y. Luo, D.K. Zhang, Surf. Coat. Technol. 334 (2018) 286–291.
[58] J.B. Cheng, Z.H. Wang, B.S. Xu, J. Thermal Spray Technol. 21 (2012) 1025–1031.
[59] Q. Fan, C. Chen, C. Fan, Z. Liu, X. Cai, S. Lin, C. Yang, Intermetallics 138 (2021) 107337.
[60] J. Yang, K. Shi, W. Zhang, Q. Chen, Z. Ning, C. Zhu, J. Liao, Y. Yang, N. Liu, W. Zhang, J. Yang, Corros. Sci. 187 (2021) 109524.
[61] H. Wan, D. Song, X. Shi, Y. Cai, T. Li, C. Chen, J. Mater. Sci. Technol. 60 (2021) 197–205.
[62] Q. Fan, C. Chen, C. Fan, Z. Liu, X. Cai, S. Lin, C. Yang, Surf. Coat. Technol. 418 (2021) 127242.
[63] G. Liang, G. Jin, X. Cui, Z. Qiu, J. Wang, Appl. Surf. Sci. 593 (2022) 153419.
[64] T. Yu, H. Wang, K. Han, B. Zhang, Vacuum 199 (2022) 110928.
[65] Y. Xu, G. Wang, Q. Song, X. Lu, Z. Li, Q. Zhao, Y. Chen, Surf. Coat. Technol. 437 (2022) 128349.
[66] A. Meghwal, A. Anupam, V. Luzin, C. Schulz, C. Hall, B. Murty, R. Kottada, C. Berndt, A. Ang, J. Alloy. Compd. 854 (2021) 157140.
[67] J. Wang, Y. Chen, Y. Zhang, W. Dai, Q. Xu, W. Li, Y. Liu, Mater. Des. 212 (2021) 110277.
[68] Q. Zhu, Y. Liu, C. Zhang, Mater. Lett. 318 (2022) 132133.
[69] S. Sun, H. Liu, J. Hao, H. Yang, J. Alloy. Compd. 886 (2021) 161251.
[70] J. Wang, Y. Chen, Y. Zhang, Y. Zhang, J. Li, J. Liu, Y. Liu, W. Li, Corros. Sci. 198 (2022) 110108.
[71] J. Xu, S. Peng, Z. Li, S. Jiang, Z. Xie, P. Munroe, H. Lu, Corros. Sci. 190 (2021) 109663.
[72] A. Shahbazkhan, H. Sabet, M. Abbasi, J. Alloy. Compd. 911 (2022) 164997.
[73] Y. Fu, C. Huang, C. Du, J. Li, C. Dai, H. Luo, Z. Liu, X. Li, Corros. Sci. 191 (2021) 109727.
[74] M.H. Allahyarzadeh, M. Aliofkhazraei, A.R.S. Rouhaghdam, V. Torabinejad, J. Alloy. Compd. 666 (2016) 217–226.
[75] B. Díaz, E. Härkönen, V. Maurice, J. Światowska, A. Seyeux, M. Ritala, P. Marcus, Electrochim. Acta 56 (2021) 9609–9618.
[76] M. Zheng, M. Sakairi, H. Jha, Corros. Sci. 55 (2012) 332–338.
[77] Z.J. Huang, D.S. Xiong, Surf. Rev. Lett. 16 (2009) 455–462.
[78] Y. Yao, S. Yao, L. Zhang, H. Wang, Mater. Lett. 61 (2007) 67–70.
[79] N.P. Wasekar, L. Bathini, L. Ramakrishna, D.S. Rao, G. Padmanabham, Appl. Surf. Sci. 527 (2020) 146896.

[80] Y. Wang, Q. Zhou, K. Li, Q. Zhong, Q.B. Bui, Ceram. Int. 41 (2015) 79–84.
[81] W. Sassi, L. Dhouibi, P. Berçot, M. Rezrazi, Appl. Surf. Sci. 324 (2015) 369–379.
[82] S. Sanjabi, A. Shirani, Mater. Corros. 63 (2012) 695–702.
[83] M. Torabi-Kaveh, M. Moshrefyfar, S. Shirzaei, S.M.A. Moosavizadeh, B. Ménendez, S. Maleki, Construct. Build. Mater. 322 (2022) 126511.
[84] W. Zhang, S. Du, B. Li, T. Mei, Y. Miao, H. Chu, J. Wang, J. Alloy. Compd. 865 (2021) 158722.
[85] O. Elianov, S. Garusi, R. Rosentsveig, S.R. Cohen, Y. Feldman, I. Pinkas, T. Bendikov, I. Kaplan-Ashiri, A. Moshkovich, V. Perfilyev, L. Rapoport, J. Moshonov, R. Tenne, B. Shay, Surf. Coat. Technol. 353 (2018) 116–125.
[86] Y. He, S.C. Wang, F.C. Walsh, Y.L. Chiu, P.A.S. Reed, Surf. Coat. Technol. 307 (2016) 926–934.
[87] X. Li, X. Yang, D. Yi, B. Liu, J. Zhu, J. Li, C. Gao, L. Wang, Intermetallics 138 (2021) 107309.
[88] Z. Zhang, B. Zhang, S. Zhu, Y. Yu, Z. Wang, X. Zhang, B. Lu, Surf. Coat. Technol. 412 (2021) 127019.
[89] Y. Pei, H. Chen, C. Wang, X. Zhan, Corrosion & Protection in Petrochemical Industry 28 (2011) No.1, 1–4+8.
[90] K. Tani, T. Kazumi, T. Tomoki, K. Yoshifumi, Y. Takatani, Y. Harada, ISIJ Int. 34 (2014) 822–828. https://doi.org/10.2355/isijinternational.34.822.
[91] J. Bao, Y. Yu, H. Liu, K. Zeng, X. Ren, Nonferrous Metals (Extractive Metallurgy) (2006) No. 4, 46–49.
[92] H. Wang, H. Lu, X. Song, X. Yan, X. Liu, Z. Nie, Corros. Sci. 147 (2019) 372–383.
[93] R. Chakrabarty, J. Song, Surf. Coat. Technol. 409 (2021) 126830.
[94] X. Qiu, N. Tariq, J. Wang, J. Tang, L. Gyansah, Z. Zhao, T. Xiong, Surf. Coat. Technol. 350 (2018) 391–400.
[95] Y. Cai, L. Zhu, Y. Cui, M. Shan, H. Li, Y. Xin, J. Han, Appl. Surf. Sci. 543 (2021) 148794.
[96] C.L. Wu, T.Z. Xu, Z.Y. Wang, C.H. Zhang, S. Zhang, C.L. Ni, D.X. Zhang, Ceram. Int. 48 (2022) 20690–20698.
[97] D. Sun, Y. Cai, L. Zhu, F. Gao, M. Shan, S. Manladan, K. Geng, J. Han, Z. Jiang, Surf. Coat. Technol. 438 (2022) 128407.
[98] Y. Cai, D. Sun, Y. Cui, S. Manladan, T. Wang, M. Shan, J. Han, Mater. Lett. 304 (2021) 130700.
[99] B. Jin, N. Zhang, S. Yin, J. Mater. Sci. Technol. 121 (2022) 163–173.
[100] S.S. Liu, M. Zhang, G.L. Zhao, X.H. Wang, J.F. Wang, Intermetallics 140 (2022) 107402.
[101] S. Zhu, Y. Yu, B. Zhang, Z. Zhang, X. Yan, Z. Wang, Mater. Lett. 272 (2020) 127870.
[102] B. Zhang, Y. Yu, S. Zhu, Z. Zhang, X. Tao, Z. Wang, B. Lu, Mater. Chem. Phys. 276 (2022) 125352.
[103] X. Yan, J. Xu, Z. Cui, B. Han, C. Zhang, Surf. Coat. Technol. 438 (2022) 128413.
[104] Y. Zou, Z. Qiu, C. Huang, D. Zeng, R. Lupoi, N. Zhang, S. Yin, Surf. Coat. Technol. 434 (2022) 128205.
[105] J. Lv, Y. Wu, S. Hong, J. Cheng, Y. Chen, J. Cheng, Z. Wei, S. Zhu, Ceram. Int. 48 (2022) 18502–18512.
[106] Z. Wei, Y. Wu, S. Hong, J. Cheng, L. Qiao, J. Cheng, S. Zhu, Ceram. Int. 47 (2021) 29410–29422.
[107] S. Grigoriev, A. Vereschaka, F. Milovich, N. Andreev, J. Bublikov, N. Sitnikov, C. Sotova, N. Kutina, Wear 486–487 (2021) 204096.
[108] T.M. Meißner, X. Montero, D. Fähsing, M.C. Galetz, Corros. Sci. 164 (2020) 108343.
[109] V. Rohr, M. Schütze, E. Fortuna, D.N. Tsipas, A. Milewska, F.J. Pérez, Mater. Corros. 56 (2005) 874–881.
[110] C. Aguzzoli, C.A. Figueroa, F.S. de Souza, A. Spinelli, I.J.R. Baumvol, Surf. Coat. Technol. 206 (2012) 2725–2731.
[111] K. Vandierendonck, M. Nesládek, S. Kadlec, C. Quaeyhaegens, M. Van Stappen, L.M.M. Stals, Surf. Coat. Technol. 98 (1998) 1060–1065.
[112] A. OrjuelaG, R. Rincón, J.J. Olaya, Surf. Coat. Technol. 259 (2014) 667–675.
[113] C. Liu, Q. Bi, A. Leyland, A. Matthews, Corros. Sci. 45 (2003) 1257–1273.
[114] E. Dobruchowska, A. Gilewicz, B. Warcholinski, L. Libralesso, D. Batory, L. Szparaga, D. Murzynski, J. Ratajski, Surf. Coat. Technol. 362 (2019) 345–354.
[115] L. Sánchez, F.J. Bolívar, M.P. Hierro, J.A. Trilleros, F.J. Pérez, Surf. Coat. Technol. 201 (2007) 7626–7634.
[116] J. Romanowska, Calphad 44 (2014) 114–118.
[117] G. Cassar, J.C. Avelar-Batista Wilson, S. Banfield, J. Housden, M. Fenech, A. Matthews, A. Leyland, Int. J. Fatigue 33 (2011) 1313–1323.
[118] Z.G. Xi, Q.F. Zhang, S.M. Jiang, G.Q. Yu, Surf. Coat. Technol. 306 (2016) 418–427.
[119] S. Kagerer, O.E. Hudak, M. Schloffer, H. Riedl, P.H. Mayrhofer, Scripta Mater. 210 (2022) 114455.
[120] M. Podgrajšek, S. Glodež, Z. Ren, Surf. Coat. Technol. 276 (2015) 521–528.
[121] Y. Teng, Y.Y. Guo, M. Zhang, Y.J. Yang, Z. Huang, Y.W. Zhou, F.Y. Wu, Y.S. Liang, Surf. Coat. Technol. 367 (2019) 100–107.
[122] S. Lu, J. Zhou, L. Wang, J. Liang, Surf. Coat. Technol. 405 (2021) 126734.
[123] Y. Jia, S. Zhu, Z. Liu, L. Yang, M. Shen, F. Wang, Corros. Sci. 180 (2021) 109184.
[124] N. Parhizkar, T. Shahrabi, B. Ramezanzadeh, Corros. Sci. 123 (2017) 55–75.
[125] Z. Liu, Q. Sun, Y. Song, J. Yang, X. Chen, X. Wang, Z. Jiang, Surf. Coat. Technol. 356 (2018) 56–63.
[126] K. Shi, L. Wang, W. Zhang, H. Chen, Z. Ning, J. Liao, Y. Yang, N. Liu, J. Yang, Fusion Eng. Des. 160 (2020) 111835.
[127] L.L. Xie, L. Wang, Y.R. Niu, T. Liu, W.L. Chen, X.B. Zheng, Z.Y. Huang, Ceram. Int. 45 (2019) 13037–13045.
[128] K.N. Xue, H.F. Lu, K.Y. Luo, C.Y. Cui, J.H. Yao, F. Xing, J.Z. Lu, Surf. Coat. Technol. 402 (2020) 126488.
[129] B.P. Singh, B.K. Jena, S. Bhattacharjee, L. Besra, Surf. Coat. Technol. 232 (2013) 475–481.
[130] R. Chakraborty, J.S. Manna, P. Saha, Surf. Coat. Technol. 363 (2019) 221–235.
[131] R. Liu, Q. Yao, L. Liu, F. Meng, F. Wang, Prog. Org. Coat. 166 (2022) 106774.
[132] X. Li, X. Liu, H. Liu, X. Liu, R. He, S. Meng, Structure, Physicochem. Eng. Aspects 639 (2022) 128345.
[133] R.R. Henriques, J. Campos, L.F.S. Calheiros, B.G. Soares, Prog. Org. Coat. 160 (2021) 106532. https://doi.org/10.1016/j.porgcoat.2021.106532.
[134] R. Han, H. He, X. Liu, L. Zhao, Y. Yang, C.B. Liu, R.C. Zeng, J. Colloid Interface Sci. 616 (2022) 605–617.
[135] B. Li, R. Bi, M. Yang, W. Gao, J. Wang, Appl. Surf. Sci. 586 (2022) 152836.
[136] M. Wu, F. Zhang, Y. Zhangyang, H. Zhang, Y. Zhao, X. Xu, M. Qin, C. Ding, J. Li, Colloid Interface Sci. Communicat. 43 (2021) 100450.
[137] F. Lu, C. Liu, Z. Chen, U. Veerabagu, Z. Chen, M. Liu, L. Hu, H. Xia, L. Cha, W. Zhang, Surf. Coat. Technol. 420 (2021) 127273.

[138] L. Ai, Y. Liu, X.Y. Zhang, X.H. Ouyang, Z.Y. Ge, Synthetic Met. 191 (2014) 41–46.

[139] J.R. Xavier, Int. J. Poly. Anal. Charact. 26 (2021) 309–329.

[140] Y.M. Liao, H.M. Shih, K.H. Hsu, C.S. Hsu, Y.C. Chao, S.C. Lin, C.Y. Chen, H.F. Meng, Polymer 52 (2011) 3717–3724.

[141] D. Verma, A. Ranga Rao, V. Dutta, Solar Energy Mater. Solar Cells 93 (2009) 1482–1487.

[142] M. Ates, J. Adhesion Sci. Technol. 30 (2016) 1510–1536.

[143] F. Gao, J. Mu, Z. Bi, S. Wang, Z. Li, Prog. Org. Coat. 151 (2021) 106071.

[144] U. Riaz, C. Nwaoha, S.M. Ashraf, Prog. Org. Coat. 77 (2014) 743–756.

[145] P.P. Deshpande, N.G. Jadhav, V.J. Gelling, D. Sazou, J. Coat. Technol. Res. 11 (2014) 473–494.

[146] Y.J. Ren, C.L. Zeng, J. Power Sources 182 (2008) 524–530.

[147] Y.J. Ren, J. Chen, C.L. Zeng, C. Li, J.J. He, Int. J. Hydrogen Energy 41 (2016) 8542–8549.

[148] Y. Hao, L.A. Sani, T. Ge, Q. Fang, Appl. Surf. Sci. 419 (2017) 826–837.

[149] A.E. Jaouhari, A.E. Asbahani, M. Bouabdallaoui, Z. Aouzal, D. Filotás, E.A. Bazzaoui, L. Nagy, G. Nagy, M. Bazzaoui, A. Albourine, D. Hartmann, Synthetic Met. 226 (2017) 15–24.

[150] S. Pour-Ali, C. Dehghanian, A. Kosari, Corros. Sci. 85 (2014) 204–214.

[151] P.J. Kinlen, V. Menon, Y. Ding, J. Electrochem. Soc. 146 (1999) 3690–3695.

[152] M.A. Deyab, J. Power Sources 268 (2014) 50–55.

[153] Z. Chen, W. Yang, B. Xu, Y. Chen, M. Qian, X. Su, Z. Li, X. Yin, Y. Liu, J. Alloy. Compd. 771 (2019) 857–868.

[154] S. Shi, Y. Zhao, Z. Zhang, L. Yu, Prog. Org. Coat. 132 (2019) 227–234.

[155] H. Li, Y. He, T. He, H. Shi, X. Ma, C. Zhang, H. Yu, Y. Bai, J. Chen, P. Luo, Appl. Surf. Sci. 549 (2021) 149227.

[156] L. Gu, S. Liu, H. Zhao, H. Yu, ACS Appl. Mater. Interf. 32 (2015) 17641–17648.

[157] S. Qiu, W. Li, W. Zheng, H. Zhao, L. Wang, ACS Appl. Mater. Interface 39 (2017) 34294–34304.

[158] B. Ramezanzadeh, M.H.M. Moghadam, N. Shohani, M. Mahdavian, Chem. Eng. J. 320 (2017) 363–375.

[159] A. Kumar, L.D. Stephenson, in: Corrosion 2002, NACE International, Denver, USA, 2002, pp. 158–160.

[160] A. Kumar, L.D. Stephenson, in: Corrosion 2003, NACE International, San Diego, USA, 2003, pp. 221–225.

[161] A. Kumar, L.D. Stephenson, in: Corrosion 2004, NACE International, New Orleans, USA, 2004, pp. 278–282.

[162] A. Kumar, L.D. Stephenson, J.N. Murray, Prog. Org. Coat. 55 (2006) 244–248.

[163] X. Li, J. Han, X. Wang, Y. Zhang, C. Jia, J. Qin, C. Wang, J.R. Wu, W. Fang, Y.W. Yang, Mater. Chem. Frontiers 3 (2019) 103–110.

[164] S.R. White, N.R. Sottos, P.H. Geubelle, J.S. Moore, M.R. Kessler, S.R. Sriram, E.N. Brown, S. Viswanathan, Nature 409 (2001) 794.

[165] C.E. Diesendruck, N.R. Sottos, J.S. Moore, S.R. White, Angewandte Chemie Int. Ed. 54 (2015) 10428–10447.

[166] D.Y. Wu, S. Meure, D. Solomon, Prog. Poly. Sci. 33 (2008) 479–522.

[167] E.N. Brown, M.R. Kessler, N.R. Sottos, S.R. White, J. Microencapsulation 20 (2003) 719–730.

[168] M.R. Kessler, N.R. Sottos, S.R. White, Compos. Part A Appl. Sci. Manufact. 34 (2003) 743–753.

[169] Y. Zhao, W. Zhang, L.P. Liao, S.J. Wang, W.J. Li, Appl. Surf. Sci. 258 (2012) 1915–1918.

[170] H. Li, Y. Cui, H. Wang, Y. Zhu, B. Wang, Colloids Surf. A Physicochem. Eng. Aspects 518 (2017) 181–187.

[171] B. Kim, T.Y. Jeon, Y.K. Oh, S.H. Kim, Langmuir 31 (2015) 6027–6034.

[172] C.J. Norris, G.J. Meadway, M.J. O'Sullivan, I.P. Bond, R.S. Trask, Adv. Funct. Mater. 21 (2011) 3624–3633.

[173] C.J. Norris, J.A.P. White, G. McCombe, P. Chatterjee, I.P. Bond, R.S. Trask, Smart Mater. Struct. 21 (2012) 094027.

[174] R.D. Farahani, K. Chizari, D. Therriault, Nanoscale 6 (2014) 10470–10485.

[175] A.M. Coppola, P.R. Thakre, N.R. Sottos, S.R. White, Compos. Part A Appl. Sci. Manufact. 59 (2014) 9–17.

[176] R.C.R. Gergely, S.J. Pety, B.P. Krull, J.F. Patrick, T.Q. Doan, A.M. Coppola, P.R. Thakre, N.R. Sottos, J.S. Moore, S.R. White, Adv. Funct. Mater. 25 (2015) 1043–1052.

[177] R.C.R. Gergely, C.W.A. Santa, B.P. Krull, E.L. Pruitt, J. Wang, N.R. Sottos, S.R. White, Adv. Funct. Mater. 28 (2018) 1870012.

[178] B.P. Krull, R.C.R. Gergely, C.W.A. Santa, Y.I. Fedonina, J.F. Patrick, S.R. White, N.R. Sottos, Adv. Funct. Mater. 26 (2016) 4561–4569.

[179] S.R. White, J.S. Moore, N.R. Sottos, B.P. Krull, W.A.S. Cruz, R.C.R. Gergely, Science 344 (2014) 620–623.

[180] X. Hao, Y. Bai, C. Ren, W. Chang, H. Qian, Y. Lou, L. Zhao, D. Zhang, X. Li, Corros. Sci. 196 (2022) 110067.

[181] Y. Yin, M. Schulz, M. Rohwerder, Corros. Sci. 190 (2021) 109661.

[182] C. Liu, H. Wu, Y. Qiang, H. Zhao, L. Wang, Corros. Sci. 184 (2021) 109355.

[183] Y. Ye, H. Chen, Y. Zou, Y. Ye, H. Zhao, Corros. Sci. 174 (2020) 108825.

[184] D. Zhang, F. Peng, J. Qiu, J. Tan, X. Zhang, S. Chen, S. Qian, X. Liu, Corros. Sci. 192 (2021) 109840.

[185] Q. Dong, J. Dai, K. Qian, H. Liu, X. Zhou, Q. Yao, M. Lu, C. Chu, F. Xue, J. Bai, Corros. Sci. 200 (2022) 110230.

[186] Y. Chen, L. Wu, W. Yao, Y. Chen, Z. Zhong, W. Ci, J. Wu, Z. Xie, Y. Yuan, F. Pan, Corros. Sci. 194 (2022) 109941.

[187] L.M. Calado, M.G. Taryba, Y. Morozov, M.J. Carmezim, M.F. Montemor, Corros. Sci. 170 (2020) 108648.

[188] L. Huang, J. Li, W. Yuan, X. Liu, Z. Li, Y. Zheng, Y. Liang, S. Zhu, Z. Cui, X. Yang, K.W.K. Yeung, S. Wu, Corros. Sci. 163 (2020) 108257.

[189] Y. Morozov, L.M. Calado, R.A. Shakoor, R. Raj, R. Kahraman, M.G. Taryba, M.F. Montemor, Corros. Sci. 159 (2019) 108128.

[190] Y. Yin, H. Zhao, M. Prabhakar, M. Rohwerder, Corros. Sci. 200 (2022) 110252.

[191] F. Zhang, P. Ju, M. Pan, D. Zhang, Y. Huang, G. Li, X. Li, Corros. Sci. 144 (2018) 74–88.